Nitrate electroreduction: recent development in mechanistic understanding and electrocatalyst design

Dong Chen [a], Di Yin [a], Shaoce Zhang [a], SenPo Yip [c], Johnny C. Ho [a, b, c, *]

[a] Department of Materials Science and Engineering, City University of Hong Kong, Hong Kong SAR 999077, China
[b] State Key Laboratory of Terahertz and Millimeter Waves, City University of Hong Kong, Hong Kong SAR 999077, China
[c] Institute for Materials Chemistry and Engineering, Kyushu University, Fukuoka 816−8580, Japan

A B S T R A C T

Ammonia, with its wide-ranging applications in global industries, plays an indispensable role in the growth and sustainability of modern society. Electrochemical nitrate reduction (eNO_3RR) presents an environmentally friendly pathway for ammonia production, sidestepping the energy consumption and greenhouse gas emissions associated with the conventional Haber−Bosch process. However, developing efficient and selective catalysts for eNO_3RR is challenging due to its intricate multiproton-coupled electron transfer process and the competing hydrogen evolution reaction. This review dives deep into the recent advancements in eNO_3RR, shedding light on the mechanism through *in situ* spectroscopic studies and innovative strategies for catalyst design. We first lay out the possible reaction pathways and products in eNO_3RR and then introduce a variety of *in situ* electrochemical characterizations that provide real-time insights into the reaction mechanism. We also explore strategies for rational electrocatalyst design to optimize the performance. Representative examples of advanced materials with high activity, selectivity, and stability are highlighted to underscore the progress made in this field. Finally, we outline emerging opportunities and future directions, such as developing multifunctional nanostructured catalysts through integrated computational and combinatorial approaches. This review aims to provide valuable insights and guidance for developing nitrate electroreduction and the efficient production of green ammonia in industry.

1. Introduction

As the world grapples with the pressing need for carbon neutrality, countries globally are in pursuit of next-generation energy technology [1]. Hydrogen, with its wide combustion limit range, low ignition energy, and rapid flame propagation speed, is emerging as a promising zero-carbon fuel of the future [2]. Green hydrogen, in particular, serves as an effective pathway to achieve carbon neutrality. However, the large-scale application of hydrogen energy faces several challenges. These include the economic constraints of electrolytic water technology, safety risks associated with storage and transportation, and slow construction of supporting infrastructure, all of which impede its commercialization process [3,4]. In light of these challenges, global attention has recently shifted toward ammonia (NH_3). As an energy storage solution, NH_3 can be catalytically decomposed to produce hydrogen, thereby addressing the issue of low-cost, long-distance transportation of hydrogen energy. It also provides a solution for the large-scale utilization of green hydrogen, further expanding the scale of the hydrogen energy industry [5,6]. From an energy perspective, ammonia's complete combustion products are only nitrogen and water, making it an ideal clean fuel substitute for coal in power systems and fossil fuels in engines [7]. Many countries actively invest in research, development, and planning of ammonia energy technology in response to this potential. Ammonia's advantages in storage and transportation are shifting its research focus from traditional agricultural fertilizer to renewable energy sources. With a high energy density (4.32 kW/h/L) and hydrogen storage capacity (17.6%), NH_3 is emerging as a potential renewable energy carrier [8]. Consequently, governments worldwide are incentivizing the development of clean ammonia synthesis, marking a significant stride toward a sustainable future.

* Corresponding author.
  E-mail address: johnnyho@cityu.edu.hk (J.C. Ho).

Traditional technology to produce ammonia is the Haber–Bosch (H–B) method, which combines N_2 and H_2 under high temperature (350–500 °C) and high pressure (150–300 atm) by using heterogeneous iron-based catalysts ($N_2 + 3H_2 \rightarrow 2NH_3$, $\Delta_f H^0 = -45.940$ kJ/mol, $\Delta_f G^0 = -16.047$ kJ/mol) [8–10]. This process is energy-intensive and not environmentally friendly because it consumes 1–2% of global energy and releases 1% of total greenhouse gases annually. More importantly, H_2 production, as the feedback of the H–B process through steam methane reforming, makes up 80% of the energy consumed [11,12]. Alternatively, electrocatalytic nitrogen (N_2) reduction (eNRR) provides possibilities to synthesize NH_3 directly from water and air under ambient conditions, which is more sustainable and environmentally friendly than the H–B process by breaking the limitation of thermodynamic equilibrium [13,14], followed by equation (1):

$$N_2 + 6H_2O + 6e^- \rightarrow 2NH_3 + 6OH^- \tag{1}$$

The process involves the hydrogenation of N_2 accomplished by consecutive proton and electron transfer, which are from the electrolyte (for proton) and the current passing through the cathode (for electron). Although the emergence of eNRR provides a solution to address the environmental pollution problems of the H–B method, it is still a relatively new and underdeveloped technology. The low solubility of N_2 in electrolytes and highly stable $N \equiv N$ bond (about 941 kJ/mol) lead to a despondent ammonia production rate [15]. The eNRR also suffers from low faradaic efficiency (FE), which is attributed to competing side reactions, such as hydrogen evolution, owing to the close standard reduction potential between HER (0 V vs. RHE) and NRR (0.09 V vs. RHE), as shown in Fig. 1a. To this end, electrochemical nitrate reduction (eNO₃RR) is emerging as an ideal alternative method for ammonia electrosynthesis, which follows equation (2):

$$NO_3^- + 6H_2O + 8e^- \rightarrow NH_3 + 9OH^- \tag{2}$$

The eNO₃RR not only has the lower bond energy of N–O (204 kJ/mol) but also the higher theoretical reaction potential (0.69 V vs. RHE) compared with NRR, making sure a high selectivity due to the wider reduction potential range without competing HER [16]. Therefore, it is much thermodynamically easier to handle relative to the eNRR process. Meanwhile, nitrate (NO_3^-) pollution poses significant harm to the environment, particularly in water systems, and can harm aquatic ecosystems and human health. At present, there are several physical and chemical treatment methods on the market, such as electrodialysis, reverse osmosis, ion exchange, etc., which can be used to collect nitrate from wastewater to obtain high-concentration nitrate brine for after treatment [17]. The eNO₃RR to high-valued NH_3 by utilizing renewable electricity is not only effective in relieving the energy and resources crisis but also helpful in the removal of nitrate pollution in wastewater. Based on the above considerations, electrochemical nitrate reduction to ammonia provides a promising solution for restoring the balance of the global nitrogen cycle, which can effectively treat nitrogen pollutants while producing NH_3 of high economic value [18]. However, during the reaction, due to the high energy of the lowest unoccupied molecular orbital π^* in NO_3^-, the charge injection into the π^* orbital is unsmooth. Therefore, the slow kinetics of the reaction is an insurmountable problem [19–21]. At the same time, the reaction process involves multiple reaction pathways and intermediates, and there are many by-products. Therefore, finding efficient and highly selective catalysts is crucial to achieve high eNO₃RR performance.

Having an in-depth understanding of the reaction mechanism is necessary to design and synthesize efficient eNO₃RR electrocatalysts, which involves four aspects, including nitrogen-containing reaction intermediates, the active sites of the catalyst, the interaction between reaction intermediates and active sites, and kinetic analysis. Although the number of works on eNO₃RR has increased rapidly these years, the performance evaluation parameters and test methods of different works are complex and varied, highlighting the difficulty of screening
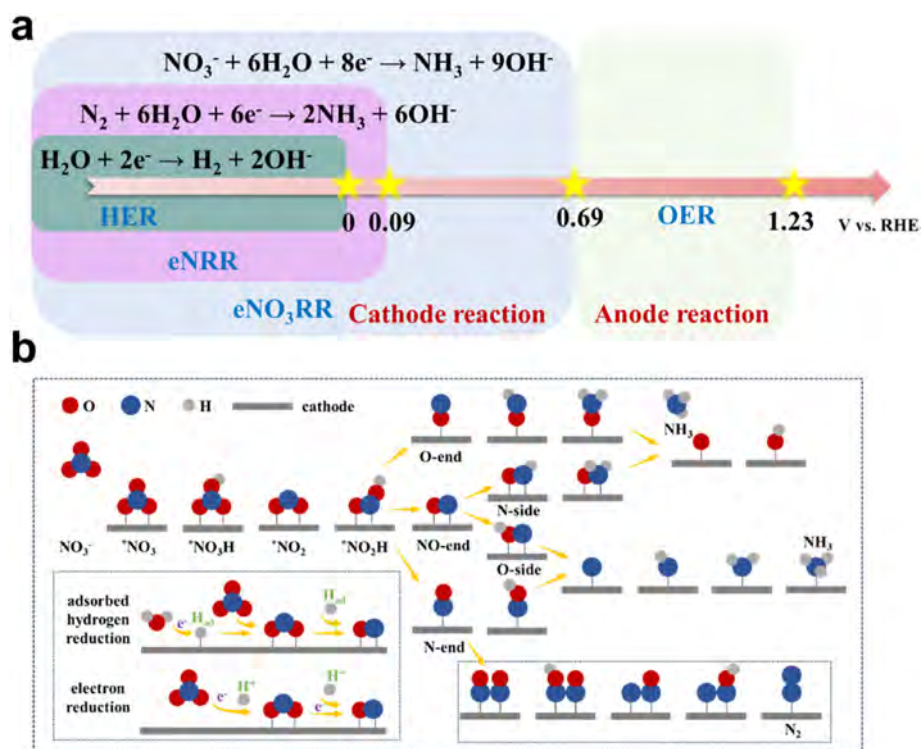
Fig. 1. The reduction potentials and possible reaction pathways of eNO₃RR. (a) Comparison of standard reduction potentials for HER, eNRR, and eNO₃RR. (b) Possible reaction pathways of eNO₃RR.

efficient materials. Therefore, there is an urgent need to summarize these works. This review first briefly summarizes the possible reaction pathways and products in eNO$_3$RR. A definite and systematic overview of various electrochemical *in situ* characterization techniques is then reviewed to help understand better the reaction intermediates and study the dynamic evolution of electrocatalysts. Next, different strategies for electrocatalyst design are summarized, which provide a mentality of designing and developing electrocatalysts with high ammonia production rates and selectivity. Finally, the review projects future development trends and challenges in this field.

2. The theoretical insight of possible pathways of eNO$_3$RR

Since the valence state of nitrogen ranges from −3 to +5, eNO$_3$RR involves a variety of reaction intermediates and products, including N$_2$ and NH$_3$, which are the most stable products, and N$_2$O, NO$_2$ which are the harmful by-products, making the reaction process complicated [22]. Theoretical investigations provide valuable insights into the possible pathways of eNO$_3$RR and help understand the underlying mechanisms involved in the reaction. As reported, the concentration of nitrate and the acidity of the electrolyte closely affect the mechanism of the electrochemical reduction of nitrate, which divides the possible pathways of eNO$_3$RR into two parts, which are the indirect autocatalytic pathway and the direct electrocatalytic reduction pathway [23−25]. When nitrate concentration is over 1 M in highly acidic environments (>1 M) in the presence of nitrite or high concentrations of nitric acid (>4 M), an indirect autocatalytic pathway will occur, in which nitrate itself is not involved in the electron transfer. The process could be described as follows:

$$HNO_3 + 2H^+ + 2e^- \rightarrow HNO_2 + H_2O \tag{3}$$
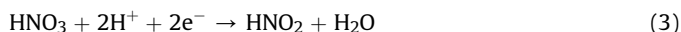
Here, nitric acid (>4 M) is a critical concentration that is thermodynamically unstable and could decompose to small amounts of HNO$_2$, NO, and NO$_2$, which means it is also in highly acidic environments [26]. In this pathway, NO$^+$ and NO$_2$ radicals are electroactive substances, further activating the autocatalytic mechanism. Based on these two electrochemically active species, the indirect reaction mechanism involves two pathways, namely the Vetter pathway and the Schmid pathway [26,27]. On the other hand, the direct electrocatalytic reduction mechanism occurs in alkaline media with relatively low nitrate ion concentrations. Conversion of nitrate-containing wastewaters to ammonia usually follows the direct electrocatalytic reduction mechanism because they contain nitrate ion concentrations below 1 M. During the direct electrocatalytic reduction process, there are three procedures: the adsorption of nitrate ions on the electrode surface, the charge transfer, and the desorption of products (Fig. 1b). To trigger eNO$_3$RR, the adsorption of nitrate ions is a crucial step. It refers to the attraction and accumulation of nitrate ions on the surface of the electrode. Bae et al. [28] have investigated the nitrate adsorption and reduction of Cu (100) in an acidic solution. *In situ* electrochemical scanning tunneling microscopy and surface-enhanced Raman spectroscopy provide valuable insights into the adsorption behavior of nitrate ions, which suggest that the Cu (100) surface is covered by nitrate molecules from the open circuit potential (OCP, 0.03 V vs. Ag/AgCl) to a potential of −0.3 V vs. Ag/AgCl, then by nitrite in the range from −0.3 to −0.5 V vs. Ag/AgCl. This work proves that adsorbed nitrite ions are an intermediate in the nitrate reduction. However, while adsorption is a crucial step, it can pose challenges. High concentrations of nitrate ions can lead to saturation of the electrode surface, limiting the efficiency of the reduction process. Furthermore, other ions in the solution, such as sulfate or

chloride ions, may compete with nitrate ions for adsorption sites on the electrode surface, potentially inhibiting the nitrate reduction process [29]. Therefore, improving nitrate adsorption at the active site within different concentrations and avoiding interference from impurity ions is one of the major challenges in eNO$_3$RR. Several strategies can be employed to optimize the adsorption process. These include modifying the electrode surface to enhance its adsorption capacity, adjusting the pH of the solution to favor nitrate ion adsorption, or applying an optimal voltage to facilitate the adsorption and reduction processes. Furthermore, materials with a high surface area or porous structure benefit from adsorbing nitrate ions [30]. In the next step, charge transfer can be carried out through electron reduction and absorbed hydrogen reduction. As shown in Fig. 3, for absorbed hydrogen reduction, water is first split to generate absorbed hydrogen atoms on the surface of the electrode. As a strong reducing agent ($E_0(H^+/H) = −2.31$ V vs. SCE), H* can be used to mitigate several intermediates, such as NO$_2$*, NO*, N*, and NH$_2$*, ultimately producing NH$_3$ or N$_2$, as equations (5) and (6). However, because forming N≡N has a higher activation energy of about 0.75 eV than that of H* (0.10 eV), and the formation of N−H bonds initiated by H* is kinetically more favorable than N−N bonds [31], NH$_3$ is more preferred to be reduced by H*.

$$H_2O + e^- \rightarrow OH^- + H* \text{ (where * represents an active site on the electrode surface)} \tag{4}$$

$$NO_3^- + 3H* \rightarrow NH_3 + 2OH^- \tag{5}$$

$$NO_3^- + 5H* \rightarrow N_2 + 3H_2O \tag{6}$$
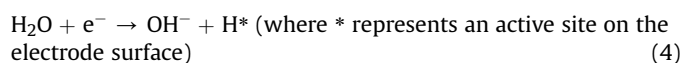
As for the electron reduction mechanism, nitrate is reduced to absorbed nitrite (NO$_2^-$) and then to N$_2$ or NH$_3$. The process involves the transfer of electrons from the electrode to the nitrate ions. This reaction pathway is generally favored under acidic conditions and requires a high overpotential (extra energy needed to drive the reaction). The steps of this reaction are as follows:

$$NO_3^- + 2H^+ + 2e^- \rightarrow NO_2^- + H_2O \tag{7}$$

$$NO_2^- + 4H^+ + 3e^- \rightarrow NH_3 + H_2O \tag{8}$$

$$NO_2^- + 6H^+ + 5e^- \rightarrow N_2 + 3H_2O \tag{9}$$

In both pathways, the choice of the electrode material can significantly affect the reaction efficiency and selectivity. For example, some metals prefer to adsorb hydrogen than nitrate ions owing to the electronic structure, like Ni, Pt, etc. [24,32,33]. In contrast, some others, like the Cu electrode [34], have a strong binding ability toward nitrate ions; these characteristics favor them catalyzing nitrate by various pathways. Consequently, such different adsorption characteristics arouse the research interest in tandem catalysts. These catalysts work cooperatively, with each catalyst performing a specific reaction step and the intermediate products formed by one catalyst serving as the reactants for the subsequent catalyst [35]. For example, in CuNi alloy, Cu prefers to bind with NO$_3^-$ while Ni quickly absorbs H$^+$, which is favorable for deoxygenation and hydrogenation in eNO$_3$RR [36]. After the NO$_3^-$ are adsorbed on the electrode surface (NO$_3$*) and then reduced to NO$_2$* and NO*, the adsorption behavior of NO*, classifying to O-end, NO-end, and N-end, determines the following reaction procedure and corresponding products. If NO* is adsorbed at the O-end, NO* undergoes further reduction to NOH* (equation 10). Subsequently, H$_2$NO* is obtained by further protonation (equation 11), and then the direct protonation leads to the production of NH$_3$ and OH$^-$ (equations 12 and 13).

$$NO* + H^+ + e^- \rightarrow NOH* \tag{10}$$

$$NOH* + H^+ + e^- \rightarrow H_2NO* \tag{11}$$

$$H_2NO* + H^+ + e^- \rightarrow NH_3 + *O \tag{12}$$

$$*O + H^+ + e^- \rightarrow OH^- \tag{13}$$
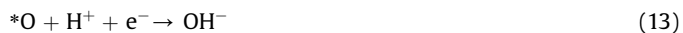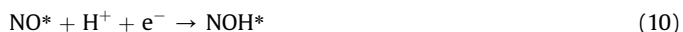
In a different scenario, when NO* is not end-adsorbed (NO−end-adsorbed), the subsequent protonation process can be categorized into two types: one where hydrogen (H) is adsorbed on nitrogen (N) and the other where hydrogen is adsorbed on oxygen (O). If the N-side is formed, the subsequent reduction will follow the same process as the O-end, proceeding by the equations (11)−(13). In the case of O−H formation, further protonation on oxygen leads to the creation of N* and water (equation 14). Subsequently, three consecutive direct protonation processes on N* produce NH*, NH_2*, and ultimately NH_3 (equations 15−17).

$$NOH* + H^+ + e^- \rightarrow N* + H_2O \tag{14}$$

$$N* + H^+ + e^- \rightarrow NH* \tag{15}$$

$$NH* + H^+ + e^- \rightarrow NH_2* \tag{16}$$

$$NH_2* + H^+ + e^- \rightarrow NH_3 \tag{17}$$
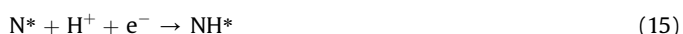
In the last type, if NO* is adsorbed at the N-end, the corresponding products strongly rely on the N−N bonding between NO* and solvated NO(aq). If an N−N bond forms between them, the reaction process will be NO*→HN_2O_2*→N_2O*→N_2OH*→N_2, accompanied by the participation of protons and electrons. In cases where there is no N−N dimerization between NO* and solvated NO(aq), NO* is further reduced to NOH* (equation 10), and the following procedures are the same as equations (14)−(17).

In summary, eNO_3RR is a complex reduction process that involves several possible reaction pathways. It faces some intrinsic challenges that impact its efficiency and practical implementation. For example, the electron reduction mechanism requires high overpotential because of nitrate's thermodynamic stability and competing reactions at the electrode surface, increasing energy consumption, and limiting the overall efficiency; the multiple possible reaction pathways lead to sluggish kinetics. Therefore, developing efficient and stable catalysts and understanding the fundamental reaction mechanisms for eNO_3RR is highly significant.

3. Electrochemical *in situ* characterizations for eNO_3RR

Since the eNO_3RR is a complicated multiproton-coupled electron transfer reaction, eNO_3RR involves a variety of reaction intermediates and products, making it a challenge to investigate the reaction mechanism. Therefore, electrochemical *in situ* characterizations are paramount in the study of eNO_3RR. Firstly, electrochemical *in situ* characterizations provide real-time information about the electrochemical processes occurring at the electrode surface during nitrate reduction [37]. This helps understand the reaction mechanisms, including intermediate species formation and their transformation pathways. Secondly, *in situ* techniques enable the identification of active sites on the catalyst surface where nitrate reduction occurs, which is vital for tailoring catalysts to maximize their catalytic activity and selectivity [38]. On the other hand, by monitoring the electrochemical behavior of catalysts in real-time, researchers can optimize the design and composition of catalyst materials for enhanced nitrate reduction performance. For example, *in situ* characterizations help evaluate the stability of

catalysts over extended periods, offering insights into degradation mechanisms, and suggesting strategies for improving durability [39]. Therefore, the continued development of electrochemical *in situ* techniques contributes to technological innovation. Advanced characterization methods, including operando spectroscopy and microscopy, enable researchers to explore new materials and techniques for nitrate reduction. In this section, some typical electrochemical *in situ* characterizations are introduced in the application of eNO_3RR.

3.1. Electrochemical in situ differential electrochemical mass spectrometry measurement

Differential electrochemical mass spectrometry (DEMS) is a powerful analytical technique that combines electrochemical methods with mass spectrometry to provide real-time information about the gas-phase products generated during electrochemical reactions [40]. In the eNO_3RR, DEMS allows for the simultaneous measurement and identification of gas-phase products generated during nitrate reduction, like NO_2, NO, and NH_3. Furthermore, by monitoring the mass spectrometric signals, DEMS enables quantitative analysis of the gas-phase products. Because of the advantages of the real-time and high sensitivity of DEMS, it allows for the identification of short-lived species that other analytical techniques might miss, so DEMS is particularly valuable for capturing transient species and reaction intermediates that may play a role in the nitrate reduction pathway [41,42].

Fig. 2a shows the general features of a DEMS device for analyzing advanced rechargeable batteries. The constitution includes inlet/outlet gas lines, a DEMS cell, a gas-detecting spectrometer, and a data-processing computer. In eNO_3RR, the DEMS instrument is the same as that of batteries except that the battery cell is replaced by an electrochemical reaction cell [43]. Therefore, when nitrate is reduced during the electrochemical reaction, the gas products are collected through the inlet/outlet line. This prevents electrolyte penetration and partitions the electrochemical reaction cell from the vacuum system for mass spectrometry. Under the vacuum system, substances vaporized are quantitatively and qualitatively measured in real-time by mass spectrometry using ion currents, and mass spectrometry data is recorded using a networked computer server. Therefore, applying *in situ* DEMS measurements in eNO_3RR offers a valuable tool for understanding the electrochemical reaction dynamics, identifying reaction intermediates, and optimizing catalysts for enhanced performance in both environmental and energy-related applications. For example, Zang et al. [44] synthesized an eNO_3RR catalyst of (NH_4)_9[Ag_9(mba)_9] nanoclusters loaded on Ti_3C_2 MXene (Ag_9/MXene). They used online DEMS for four cycles to detect the gas products under the potential from 0.05 to −0.95 V vs. RHE (5 mV/s). The mass-to-charge (m/z) signals of 30, 17, 16, and 15 that correspond to NO, NH_3, NH_2, and NH are shown in Fig. 2b, respectively. Additionally, m/z signals of 2 come from H_2, generated from the competitive HER. Furthermore, in the work from Shao et al. [45], besides the signals of 17 that represent the NH_3 product, the weak m/z signals of 2 and 30 are contributed to H_2 and NO (Fig. 2c). Looking at the y-axis scale bar, it is reasonable that the signal intensity of NO is lower than that of H_2 by several orders of magnitude because GC cannot quantify the NO. The results indicate the excellent NH_3 production efficiency and selectivity of the ordered hollow CoP nanosphere assembled on a self-supported carbon nanosheet array (CoP−CNS). As mentioned, online DEMS is a promising tool for confirming the reaction pathways and intermediates of eNO_3RR. Yu et al. [46] found the appearance of NO, NH_2OH, and NH_3 due to the m/z signals of 30, 33, and 17 (Fig. 2d). They thus confirmed the reaction pathways of Cu clusters/TiO_{2-x} with abundant oxygen vacancies during electrocatalytic nitrate reduction to ammonia. They
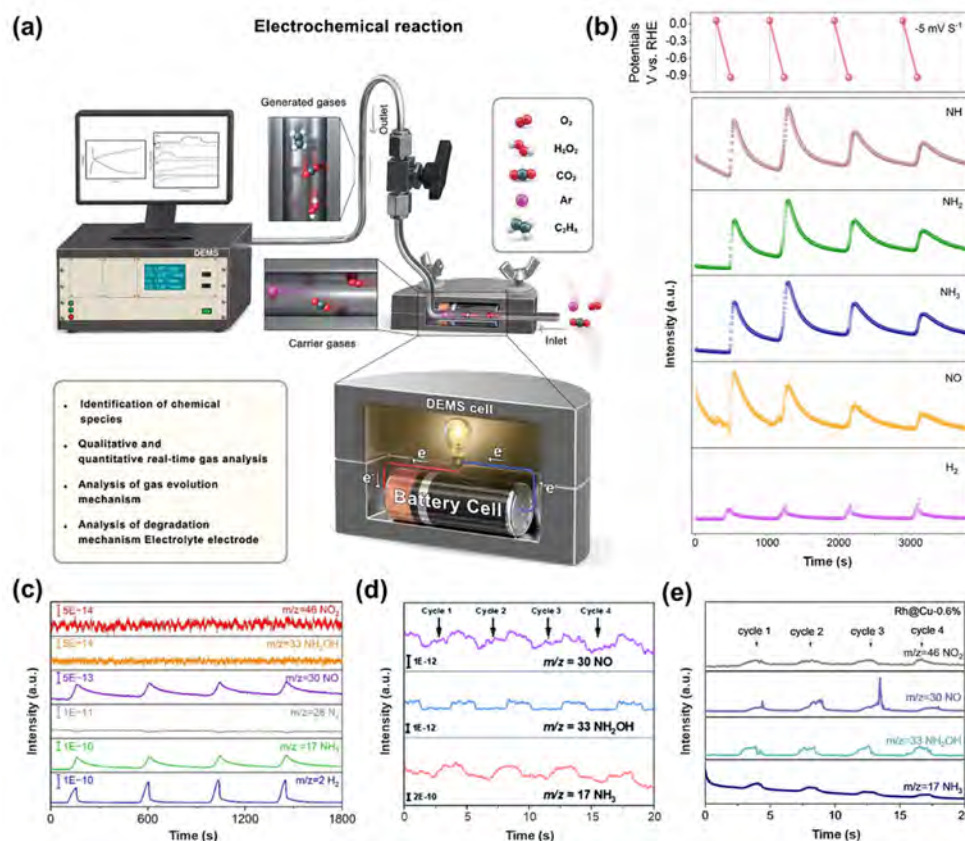
Fig. 2. The application of electrochemical *in situ* DEMS measurement in eNO$_3$RR. (a) Schematic diagram of a DEMS device, including inlet/outlet gas lines, a DEMS cell, a gas-detecting spectrometer, and a data-processing computer. Reproduced with permission [43]. Copyright 2023, John Wiley and Sons. *In situ* DEMS analysis in electrocatalytic eNO$_3$RR process: (b) Ag$_9$/MXene. Reproduced with permission [44]. Copyright 2024, John Wiley and Sons. (c) CoP−CNS. Reproduced with permission [45]. Copyright 2022, Springer Nature. (d) 10Cu/TiO$_{2-x}$. Reproduced with permission [46]. Copyright 2022, Royal Society of Chemistry. (e) Rh@Cu−0.6%. Reproduced with permission [47]. Copyright 2022, John Wiley and Sons.

carried out the density functional theory (DFT) calculations to simulate the interaction between reactive intermediates and active species, revealing the active origin of the catalysts. Moreover, Luo et al. have comprehensively described the reaction mechanism by online DEMS on copper-supported rhodium clusters and single-atom catalysts (Fig. 2e) [47]. From 0.78 V to −1.42 V vs. RHE, four cycles all show the signals of 46, 30, 33, and 17, corresponding to NO$_2$, NO, NH$_2$OH, and NH$_3$, respectively. Therefore, the reaction process has been confirmed to include the deoxygenation reactions (*NO$_3$ → *NO$_2$ → *NO) and hydrogenation steps (*NO → *NOH →*NH$_2$OH → *NH$_3$).

Therefore, DEMS allows for directly detecting and quantifying the volatile intermediates/products in eNO$_3$RR by coupling an electrochemical cell with a mass spectrometer. By monitoring on-line signals like NO, N$_2$O, and NH$_3$, DEMS enables researchers to study the temporal evolution of these species, understand their relationship with reaction conditions (such as electrode potential, electrolyte composition, and temperature), and optimize the electrochemical process for enhanced selectivity and efficiency.

3.2. Electrochemical in situ fourier-transformed infrared spectroscopy (FTIR) measurement

FTIR is a powerful analytical technique that can provide valuable insights into nitrate reduction, especially detecting the formation and depletion of reaction intermediates and products that may be too short-lived to capture through conventional *ex situ* analysis

after a reaction is stopped [48]. Infrared radiation consists of electromagnetic waves corresponding to the vibrational frequencies of chemical bonds in samples. When infrared light is directed onto a sample, it is absorbed by the molecules, causing them to vibrate. These vibrational modes are specific to different chemical bonds and thus provide characteristic spectral features in the infrared region [49]. FTIR has several advantages: i) it allows for real-time and non-destructive analysis of the reaction mixture, enabling researchers to monitor the progress of eNO$_3$RR without the need for sampling and subsequent analysis. This capability provides a unique opportunity to study the reaction kinetics and identify intermediate species involved. ii) FTIR provides molecular-level information about the functional groups present in the reaction mixture. By tracking the infrared absorption bands corresponding to nitrate, nitrite, ammonium, and other nitrogen-containing species, scientists can monitor the step-wise mechanism of eNO$_3$RR. The technique has helped identify rate-limiting steps and shed light on the role of the catalyst under working conditions. iii) *in situ* FTIR measurement allows for the study of nitrate reduction under realistic conditions. It enables the analysis of nitrate reduction in the presence of various catalysts, such as metal nanoparticles or enzymes, which can enhance the reaction rate or selectivity. By monitoring the changes in the FTIR spectra, researchers can determine the effect of different factors on the reaction and optimize the performance of catalysts [50,51]. However, it is essential to note some limitations to applying *in situ* FTIR measurement in eNO$_3$RR. One limitation is the need for a suitable IR-transparent

window material to withstand the reaction conditions. Additionally, some reaction products or intermediates involved in eNO₃RR may be present at low concentrations or have weak or low-intensity vibrational modes, making their detection and characterization challenging [52]. Furthermore, FTIR spectra can exhibit a wide range of peaks due to the presence of different molecular species and functional groups and background interference, such as water vapor or CO₂ absorption bands. This can make the analysis and interpretation of the spectra difficult, particularly when multiple species are present simultaneously or when overlapping peaks occur.

As shown in Fig. 3a, the FTIR spectrometer consists of an infrared source and detector, which includes the sample compartment [53]. Loh et al. [54] performed the *in situ* FTIR in 0.01 M nitrate. Only peaks of *NO₃, *NO₂, and *NO are detected on Cu₂O. In contrast, additional peaks of *NHO, *NH₂OH, and *NH₃ are observed over Ru/Cu₂O, but *NO₃ disappeared (Fig. 3b and c),

which suggests the positive effect of Ru nanoparticles that help to match the rate of HER and eNO₃RR kinetics to favor hydrogen transfer by nitrate ions, leading to a substantially improved electrocatalytic performance. To better analyze the *in situ* FTIR, the spectrums were usually processed by the formula of $\Delta R/R = (R_S - R_{ref})/R_{Ref}$ (R_S, R_{Ref} represent the spectrum collected at reference potential and working potentials, respectively) [55,56]. Consequently, the downward and upward peaks suggest the formation and consumption of reaction intermediates and NO_3^-, respectively. Chu et al. [57] utilized *in situ* FTIR to gain more insights into the eNO₃RR mechanism on their MBene catalyst of FeB₂ (Fig. 3d−f). From open circuit potential to −0.6 V vs. RHE, the more apparent downward peak centered at 1350 cm⁻¹ indicates the consumption of NO_3^- over FeB₂. In contrast, five upward peaks appear along with the decrease of potential, including deoxidation intermediate (-NO₂ at 1250 cm⁻¹), hydrogenation intermediates (−NHₓ at 1100−1160 cm⁻¹, −NH₂ at 1280 cm⁻¹, H−N−H at 1420 cm⁻¹) and
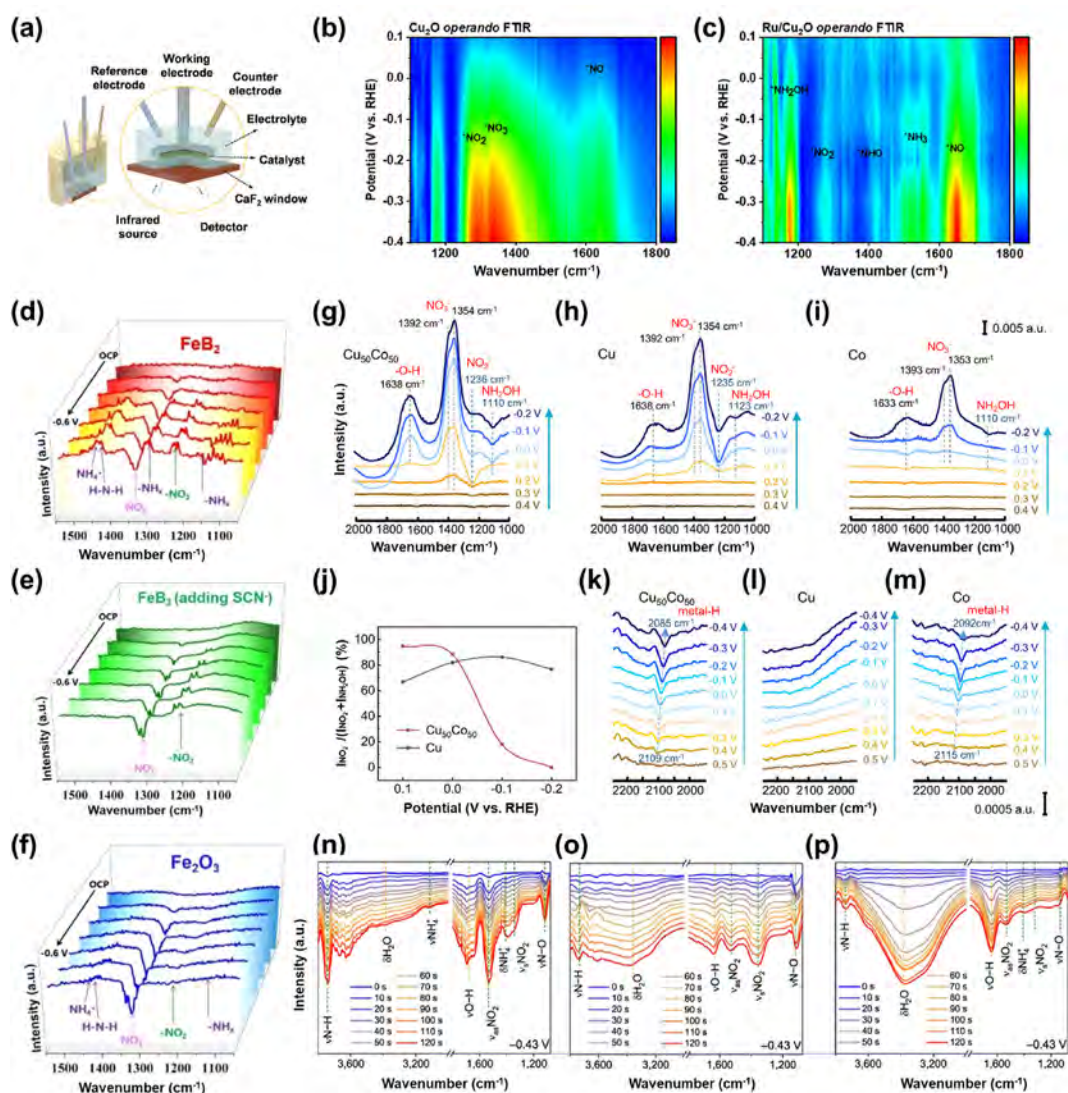
Fig. 3. The application of electrochemical *in situ* FTIR measurement in eNO₃RR. (a) Schematic diagram of the experimental set-up for *in situ* FTIR measurement. Reproduced with permission [53]. Copyright 2023, John Wiley and Sons. (b, c) *In situ* FTIR for nitrate reduction on Cu₂O and Ru/Cu₂O surface in an electrolyte containing 1.0 M KOH and 0.01 M KNO₃ (the notation for the color bar corresponds to intensity value). Reproduced with permission [54]. Copyright 2023, American Chemical Society. (d−f) Potential-dependent *in situ* FTIR spectra of FeB₂, FeB₂ (with SCN⁻ addition in the electrolyte) and Fe₂O₃. Reproduced with permission [57]. Copyright 2023, John Wiley and Sons. (g−i) Potential-dependent *in situ* FTIR spectra of Cu₅₀Co₅₀, Cu, and Co. (j) $I_{NO2-}/(I_{NO2-} + I_{NH2OH})$ ratio at different electrode potentials. (k−m) ATR-FTIR spectra on Cu₅₀Co₅₀, Cu, and Co in 1.0 M KOH. Reproduced with permission [58]. Copyright 2022, Springer Nature. (n−p) Time-dependent *in situ* FTIR spectra of CoP−CNS and Co−CNS in 1.0 M OH⁻ with 1.0 M NO₃⁻, and CoP−CNS in 1.0 M OH⁻ with 10 mM NO₃⁻. Reproduced with permission [45]. Copyright 2022, Springer Nature.

generated NH_3 (NH_4^+ at 1450 cm^{-1}) [17]. Then, the Fe_2O_3 catalyst was synthesized to investigate the effect of individual Fe sites in the reaction mechanism. SCN was added to the electrolyte to poison the Fe sites and study the B site. As shown in Fig. 3f, the FTIR of FeB_2 under the existence of SCN$^-$ in the electrolyte shows almost only two nitrogen oxide species. At the same time, the hydrogenation intermediates nearly disappear, confirming the function of the Fe site in providing *H in the hydrogenation process. Meanwhile, all the characteristic peaks of deoxidation/hydrogenation intermediates are weak over Fe_2O_3 catalysts, suggesting the sluggish eNO$_3$RR kinetics and energetics of Fe sites. It concludes that B and Fe in FeB_2 play a synergistic role in the eNO$_3$RR process. In another work, Sun et al. [58] measured the *in situ* FTIR on $Cu_{50}Co_{50}$ (Cu/Co molar ratio of ca. 50/50), Cu, and Co in the potential range from 0.4 to −0.2 V (Fig. 3g−m). In addition to the peaks of N−O symmetric and asymmetric stretching assigned to consumed NO_3^- and N−O antisymmetric stretching of formed NO_2^-, −N−O− stretching vibration of hydroxylamine (NH_2OH) are also observed when the potential was negatively moving over 0.1 V [59−61]. Furthermore, a peak located around 1638 cm^{-1} is contributed by water electrolysis. The higher intensity of this peak over $Cu_{50}Co_{50}$ than pristine Cu and Co indicates the faster hydrogen generation involved in the hydrodeoxidation of NO_3^-. By calculating the band intensity of $I_{NO2-}/(I_{NO2-} + I_{NH2OH})$ between $Cu_{50}Co_{50}$ and Cu, they demonstrate that alloying Cu with Co could profoundly enhance the hydrogenation of *NO_2 to the final product NH_3, thus achieving the highly eNO$_3$RR activity of $Cu_{50}Co_{50}$. Similarly, Shao et al. [45] used the time-dependent *in situ* FTIR to prove that the eNO$_3$RR is more favorable than the HER over CoP−CNS within a broadened reaction window (Fig. 3n−p). More importantly, they confirm the CoP CNS catalysts always consume adsorbed H (H_{ads}) promptly by comparing the band intensity of N−H and O−H peaks.

Besides the conventional *in situ* FTIR measurement, *in situ* attenuated total reflection-Fourier transform infrared spectroscopy (ATR-FTIR) is a more versatile and powerful technique for analyzing various materials. Compared to conventional FTIR spectroscopy, the sample is brought into direct contact with an ATR crystal in ATR-FTIR spectroscopy, which is typically made of a high refractive index material such as diamond, germanium, or zinc selenide, rather than generally analyzed by passing the infrared beam through it [62]. This crystal acts as both the sampling element and the internal reflection element. When the infrared beam is directed onto the ATR crystal at a specific angle, it undergoes total internal reflection, resulting in an evanescent wave that extends into the sample. This evanescent wave interacts with the molecules at the sample-ATR crystal interface, causing them to absorb infrared radiation and vibrate. After interaction with the sample, the attenuated infrared beam is then collected and measured by a detector, generating an ATR-FTIR spectrum. Therefore, the ATR-FTIR technique allows for the analysis of a wide range of sample types, including liquids, solids, and even thin films, without the need for time-consuming sample preparation and is more sensitive to the signal of adsorbed species on catalysts' surfaces [63]. For instance, Fig. 3k−m shows ATR-FTIR spectra on $Cu_{50}Co_{50}$, Cu, and Co in 1.0 M KOH, which show the peaks of the adsorbed proton (*H) on the surface of catalysts. The negative shift from the band around 2109 cm^{-1} at 0.5 V to 2085 cm^{-1} at −0.4 V is assigned to the Stark turn rate of 26.7 cm^{-1}/V [64,65]. In the electrolyte without NO_3^-, the apparent peak signal in $Cu_{50}Co_{50}$ and Co but absent peak on Cu indicates that *H on $Cu_{50}Co_{50}$ is mainly attributed to water dissociation on Co sites. In summary, the application of *in situ* FTIR spectroscopy has provided valuable molecular-level insights into eNO$_3$RR. It remains a powerful tool to probe reaction intermediates and mechanisms under working conditions.

3.3. Electrochemical in situ electron spin resonance measurement

Electron spin resonance (ESR) spectroscopy, also called electron paramagnetic resonance (EPR) spectroscopy, is particularly useful for studying reactions involving free radicals or transition metal ions, providing information about their electronic structure, spin states, and local environments [66]. *In situ* ESR spectroscopy is a powerful technique for investigating and characterizing paramagnetic species in chemical reactions and biological systems. One specific application of *in situ* ESR spectroscopy is the study of the spin trap of hydrogen radical by 5,5-dimethyl-1-pyrroline N-oxide (DMPO) during eNO$_3$RR [67,68]. DMPO is a commonly used spin trap that can capture and stabilize short-lived radicals formed during various chemical reactions, including the reduction of nitrate to ammonia. During eNO$_3$RR, reactive nitrogen species such as nitric oxide (NO·) and nitrogen dioxide (NO$_2$·) can be produced as intermediates. These highly reactive species can participate in redox reactions or radical-mediated processes. The DMPO-H spin trap can react with these radicals, forming stable DMPO radical adducts, which ESR spectroscopy can detect and characterize [69]. *In situ* ESR spectroscopy allows for the real-time monitoring of the formation and decay of DMPO radical adducts during the eNO$_3$RR. By continuously measuring the ESR spectra, researchers can gain insights into the kinetics, reaction mechanisms, and intermediates involved in the process. Chu et al. [70] carried out ESR spectroscopy to evaluate the amounts of generated/consumed *H (Fig. 4a−f). Nine ESR signals could be obtained with an intensity ratio of 1:1:2:1:2:1:2:1:1, and the ratio is consistent with the hyperfine coupling constants calculated as αN = 16.3 G and αH = 22.5 G, which are assigned to the signal of DMPO-H [71,72]. Without NO_3^- in the electrolyte, both Pd and RuO$_x$/Pd show a strong DMPO-H signal, but RuOx/G has a weak intensity. In contrast, all the DMPO-H signals decrease after adding NO_3^- in the electrolyte, especially for RuOx/Pd and RuOx/G, which are barely detected. The results demonstrate the more excellent capability of Pd compared to graphene in producing abundant *H but the weaker eNO$_3$RR activity than RuO$_x$/Pd and RuO$_x$/G in consuming *H to boost the eNO$_3$RR hydrogenation reaction. Then, the authors investigate the relationship between NO_3^- concentration and DMPO-H signals to quantify the hydrogenation capability (H_C), which is defined as the EPR intensity attenuation amplitude divided by the reaction time and NO_3^- concentration of a catalyst for the eNO$_3$RR. As shown in Fig. 4c−f, Zhi et al. [73] studied the EPR of Ru/BTO-OV$_1$ catalyst collected under different ultrasonic intensities. They found an improved DMPO-H signal with the increased ultrasonic intensity upon constant NO_3^- concentration (0.05 M), verifying the more produced NO_3^- owing to the water electrolysis by bubbles collapse triggered by piezoresponse (Fig. 4g). Interestingly, by monitoring the concentration of *H through DMPO, they compared the current densities of eNO$_3$RR with and without DMPO under different ultrasonic intensities, in which all the eNO$_3$RR currents described significantly decreased due to the consumption of *H after introducing DMPO (Fig. 4h). Similar work on EPR measurement is shown in Fig. 4i, which is from Shao's group [45]. With increased NO_3^- concentration, the DMPO-H signal intensity decreases and eventually disappears when the concentration reaches 1.0 M.

In addition to exploring the existence of *H, *in situ* ESR spectroscopy can also provide quantitative data about the concentration of the trapped radicals [74]. By comparing the ESR signal intensity of the DMPO radical adducts to that of a known standard, researchers can estimate the concentration of the radicals, providing insights into their formation and consumption kinetics during the nitrate reduction process. However, as *in situ* ESR spectroscopy offers a powerful tool for investigating the formation and behavior of reactive radicals mainly when applied to the DMPO-H spin trap
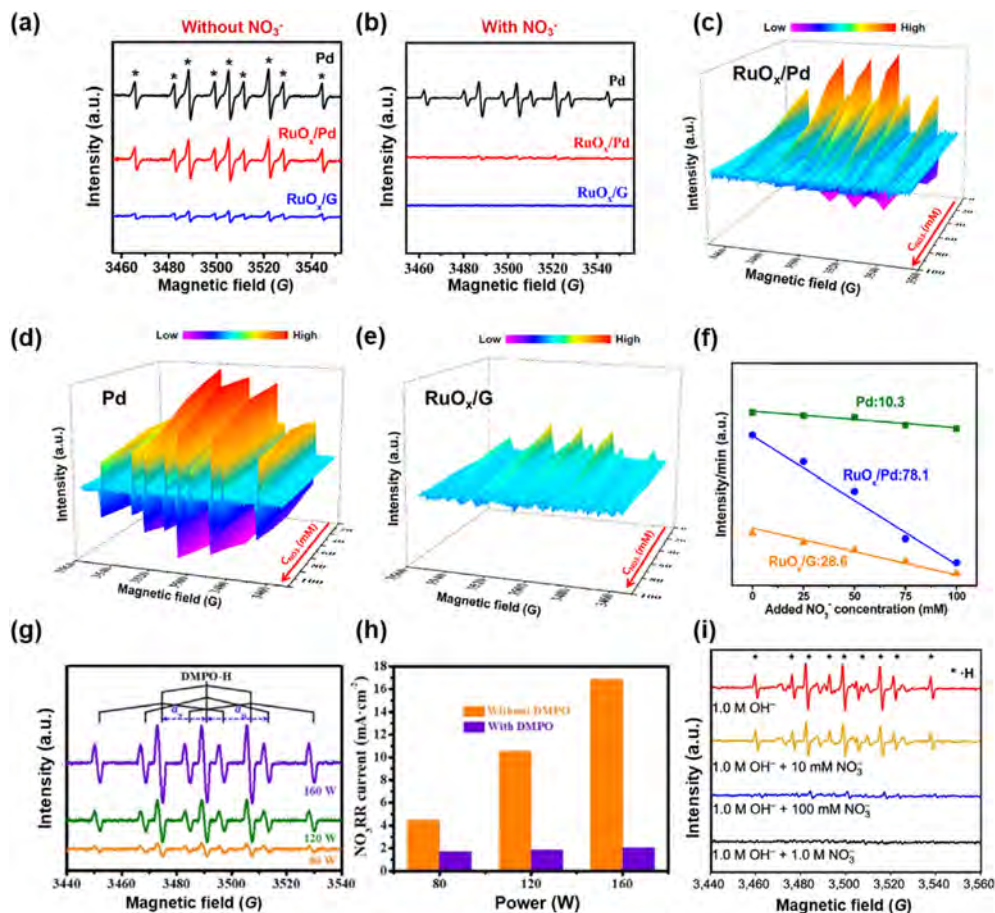
Fig. 4. The application of electrochemical *in situ* ESR measurement in eNO₃RR. (a, b) DMPO-involved ESR spectra with and without NO₃⁻ (each line is collected after 5 min of electrolysis at −0.5 V vs. RHE). (c−e) DMPO-involved ESR spectra of RuOₓ/Pd, Pd, and RuOₓ/G at different NO₃⁻ concentrations, and (f) corresponding fitted lines of ESR intensity/ reaction time vs. NO₃⁻ concentration. Reproduced with permission [70]. Copyright 2023, American Chemical Society. (g) DMPO-involved ESR spectra of Ru/BTO-OV₁ in 0.05 M NO₃⁻ + 0.1 M PBS under Ar with various ultrasonic power (W). (h) eNO₃RR current density measured with and without DMPO. Reproduced with permission [73]. Copyright 2023, Elsevier. (i) DMPO-involved ESR spectra of the CoP−CNS in the solution with different NO₃⁻ concentrations. Reproduced with permission [45]. Copyright 2022, Springer Nature.

in eNO₃RR, ESR is unsuitable for the electron-mediated pathway. In the electron-mediated pathway, the eNO₃RR occurs through multiple electron transfers between the electrode and the nitrate species without the direct involvement of paramagnetic species. The reactive intermediates formed in this pathway are typically short-lived and do not possess unpaired electrons, which are necessary for ESR detection.

3.4. Electrochemical in situ Raman spectra

In situ Raman spectroscopy is a non-destructive spectroscopic technique used to study materials' molecular structure and chemical changes. It is based on the phenomenon of Raman scattering and obtains information by measuring the spectrum scattered by a sample [75]. As illustrated by the set-up for *in situ* Raman measurement in Fig. 5a, Raman spectroscopy usually uses lasers as the excitation light source. Laser has high monochromaticity and high light intensity, which can provide sufficient photon energy to excite molecular vibrations in the sample. Some laser photons interact with molecules when laser light shines on a sample. The photon's energy can change during this process, producing Raman scattered photons. The energy of Raman-scattered photons can be higher or lower than the energy of the incident light, depending on the vibrational modes of the molecules in the sample. There is a correspondence between the energy of Raman-scattered photons and the vibration frequency of the molecules in the sample. When a

molecule vibrates, it absorbs or releases energy, causing the Raman scattered photons to shift in frequency. This frequency shift, a Raman shift, provides information about the molecular structure and chemical environment [76]. For electrochemical *in situ* Raman measurement, the electrochemical cell is the central part, which consists of three electrodes (working electrode, counter electrode, and reference electrode) and an electrolyte solution. Therefore, information about the molecular vibration modes, the nature of chemical bonds, and the crystal structure in the sample can be obtained by analyzing the *in situ* Raman spectrum [77]. Electrochemical surface-enhanced Raman spectroscopy (SHINERS) has recently appeared and allows for *in situ* characterization and analysis of electrochemical processes and detecting trace-level analytes with high sensitivity [78]. It involves enhancing Raman signals through the interaction of molecules with metallic nanostructures. When molecules are adsorbed on the surface of these nanostructures, the localized surface plasmons in the metal induce a substantial enhancement of the electromagnetic field, leading to a significant amplification of the Raman-scattering signal. This enhancement enables the detection of molecules at deficient concentrations and provides detailed information about their chemical structure and environment. When applied to nitrate reduction catalysis, *in situ* Raman spectroscopy or SHINERS spectra could provide a wealth of insights for nitrate, nitrite, surface oxides, and other species, helping researchers to correlate catalyst structures to activity in real-time [79]. Fig. 5b−c shows the work from Sun et al.
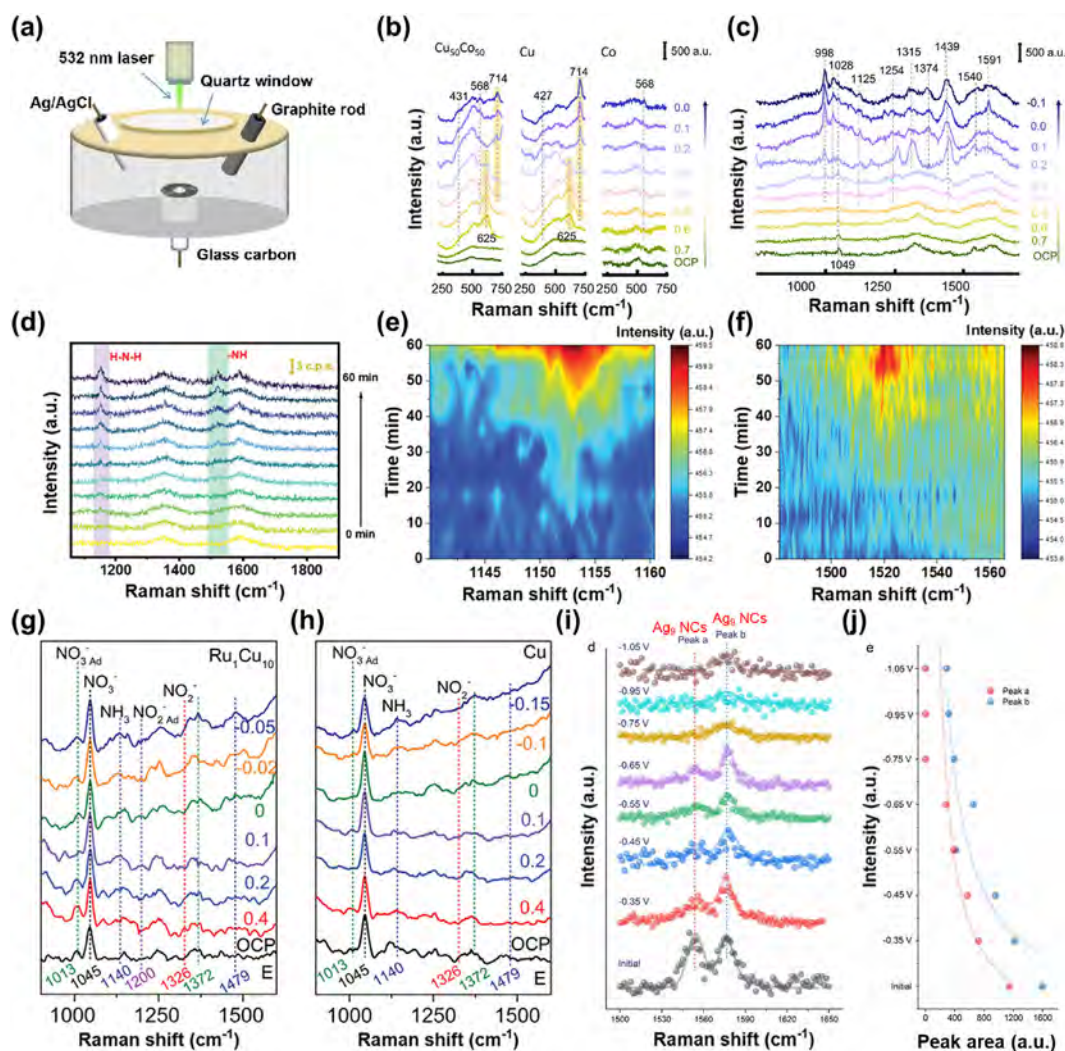
Fig. 5. The application of electrochemical *in situ* Raman measurement in eNO$_3$RR. (a) Schematic diagram of the experimental set-up for *in situ* Raman measurement. Reproduced with permission [76]. Copyright 2023, John Wiley and Sons. (b, c) SHINERS spectra between 230 and 750 cm^{-1} and 750−1700 cm^{-1} on Cu$_{50}$Co$_{50}$, Cu, and Co in 0.1 M KNO$_3$ + 0.01 M KOH. Reproduced with permission [58]. Copyright 2022, Springer Nature. (d) *In situ* Raman spectra of Pt$_{0.9}$/Ce$_{0.5}$-SS collected at −0.5 V vs. RHE in 0.5 M Na$_2$SO$_4$ + 0.1 M KNO$_3$, and (e, f) corresponding contour plots of the color background area in (d). Reproduced with permission [82]. Copyright 2023, John Wiley and Sons. (g, h) *In situ* Raman spectra of Ru$_1$Cu$_{10}$ and Cu in 0.1 M KNO$_3$ + 1.0 M KOH. Reproduced with permission [85]. Copyright 2023, John Wiley and Sons. (i) *In situ* Raman spectra of Ag$_9$ NCs in 0.5 M K$_2$SO$_4$ + 200 ppm NO$_3^-$-N, and (j) corresponding relation between potential and peak area. Reproduced with permission [44]. Copyright 2024, John Wiley and Sons.

[58]. They measured the SHINERS spectra between 230−750 cm^{-1} and 750−1700 cm^{-1} on Cu$_{50}$Co$_{50}$, Cu, and Co. The gradual decreased peak signal around 625 cm^{-1} demonstrates the reduction of Cu$_2$O to Cu. The bands at 431 cm^{-1} and 568 cm^{-1} assigned to Cu-O$_x$ and Co-O$_x$ indicate the adsorption of oxynitride on the catalyst's surface [80]. In addition, the spectra between 750 and 1700 cm^{-1} collected as the potential decreased from 0.7 to −0.1 give abundant information on the surface chemical intermediates. For instance, the bands centered at 1540 cm^{-1} and 1591 cm^{-1} represent the appearance of HNO and HNH species [81]. When the potential negatively shifted further to 0.1 V, the vanishing of HNO but the appearance of HNH verified the efficient conversion from nitrate to ammonia by hydrodeoxidation. Our previous work reported that 2D SnS nanosheets with tailored interlayer spacing are an efficient eNO$_3$RR catalyst [82]. This was confirmed by *in situ* Raman spectra (Fig. 5d−f). As time passed, the peaks at 1152.5 and 1521.4 cm^{-1} assigned to the H−N−H and N−H bond gradually appeared on Pt$_{0.9}$/Ce$_{0.5}$-SS, demonstrating the reduction of nitrate [83,84]. In Li et al.'s work [85], the band of aqueous NO$_3^-$ and the adsorbed NO$_3^-$ (NO$_3^-$$_{Ad}$) are centered at 1045 cm^{-1} and 1013/

1372 cm^{-1}, respectively (Fig. 5g and h) [86−88]. They used the intensity ratio of I$_{1013}$/I$_{1045}$ to quantify the adsorption capability of NO$_3^-$ on Ru$_1$Cu$_{10}$ and Cu. Moreover, the additional peak ascribed to adsorbed NO$_2^-$ (1200 cm^{-1}) and the appearance of NH$_3$ (1140/ 1479 cm^{-1}) on Ru$_1$Cu$_{10}$ compared with Cu further indicates the quick conversion from NO$_3^-$ to NO$_2^-$, and eventually transfer to NH$_3$.

In addition to getting information on reaction intermediates during eNO$_3$RR, *in situ* Raman spectroscopy provides valuable information about materials' physical properties and structural changes. For example, it can study phase transitions, polymorphism, solid-state reactions, and crystallization processes [89]. By tracking shifts in Raman peaks, changes in peak intensities, or the appearance of new peaks, researchers can deduce structural transformations, phase transitions, or modifications in the lattice structure of materials. Zang et al. [44] prepared (NH$_4$)$_9$[Ag$_9$(mba)$_9$] nanoclusters (Ag$_9$ NCs) loaded on Ti$_3$C$_2$ MXene for highly efficient eNO$_3$RR. *In situ* Raman spectra were conducted to track the structure change of the catalyst. As shown in Fig. 5i and j, two characteristic peaks contributed by the Ag$_9$ center at 1551 cm^{-1} (peak a) and 1576 cm^{-1} (peak b) gradually disappeared with a potential

negative shift. The calculated peak area has a downward non-linear relationship with applied potential, confirming the structure transformation of Ag_9 NCs during the eNO_3RR process. However, Raman spectroscopy is susceptible to fluorescence interference, particularly when analyzing complex samples or species with strong fluorescence. Fluorescence emission can overlap with Raman scattering, reducing the quality of the Raman signal and making it challenging to accurately identify and analyze specific species. Similar to FTIR spectra, Raman spectra can exhibit spectral overlapping, where multiple species contribute to the observed signals. Also, the spatial resolution of Raman spectroscopy is limited by diffraction, typically in the range of micrometers. This may limit the ability to probe localized regions or specific sites on the electrode surface, especially in systems with high surface roughness or inhomogeneity. Overall, in situ Raman spectroscopy is a valuable tool for studying chemical reactions, materials transformations, and structural changes in real-time and provides molecular-scale details that have significantly enhanced understanding of nitrate reduction pathways and catalysis.

3.5. Electrochemical in situ X-ray absorption spectroscopy measurement

X-ray absorption spectroscopy (XAS) is a powerful technique for studying materials' structural and electronic changes during electrochemical processes. Unlike FTIR, ESR, and Raman spectroscopy techniques that provide valuable insights into reaction intermediates, XAS measurement could directly probe the catalytic active sites and analyze the local geometric and electronic structure around select element absorbers, often the catalytic metal centers [90]. Compared with conventional ex situ XAS, which only captures snapshots and may miss transient surface structures during catalysis, in situ XAS measurements combine electrochemical cells and XAS. They could be conducted under working reaction conditions [91]. The electrochemical cell typically consists of a working electrode, a reference electrode, and a counter electrode immersed in an electrolyte solution containing nitrate ions. XAS spectroscopy involves the characterization of the absorption of X-rays by the sample as a function of incident X-ray energy. In the case of eNO_3RR, XAS is usually performed using X-ray absorption near-edge structure (XANES) and extended X-ray absorption fine structure (EXAFS) techniques. During the electrochemical in situ XAS experiment, X-rays are directed toward the working electrode, and the absorption spectrum is recorded by applying various potentials. By monitoring the XANES and EXAFS spectra, structural changes, oxidation states of the element, oxidation state shifts, ligand rearrangements, and strain effects that directly impact catalytic activity and selectivity involved in the nitrate reduction process can be identified, providing an in-depth understanding of the formation of reaction intermediates, the stability of active sites, and the evolution of the electrochemical reaction over time [92]. Electrochemical in situ XAS has been successfully applied to investigate the eNO_3RR on various electrode materials, such as metal catalysts, metal oxides, and carbon-based materials. For example, Zhang et al. [93] studied the potential-driven Cu single atoms restructure to nanoparticles during eNO_3RR by in situ XAS technique. From fresh to -0.1 V vs. RHE, Cu^{2+} was quickly reduced to Cu^+/Cu^0 (Fig. 6a and b). More Cu^0 occurred with the increased applied potential. They also found a similar change trend between the Cu^0 percentage and the faradaic efficiency of NH_3 (FE_{NH_3}), indicating the correlation between catalytic selectivity and Cu^0 percentage (Fig. 6c). Moreover, the Fourier transforms of the EXAFS (FT-EXAFS) spectra demonstrated the Cu−N bond was partially broken in Cu−N_4 structure during eNO_3RR and Cu was transferred from a single atom to nanoparticle upon negative potential (Fig. 6d). Continuing

measuring the EXAFS and XANES spectra of the samples, the results suggest that large Cu NPs re-dispersed to single atoms through $[Cu(OH)_4]^{2-}$ intermediates, which are subsequently trapped by pyridinic nitrogen on the carbon support in oxygen and/or water-contained oxidative environments (Fig. 6e and f) [94−96]. Therefore, through electrochemical in situ XAS measurement, the mechanism of Cu single atoms in Cu−N_4 structure behind eNO_3RR has been demonstrated, in which the Cu single atoms aggregated to nanoparticles driven by negative applied potential during the reduction process and then reversed back in oxidation environment (Fig. 6g). Researchers generally believe the Cu−N_x single-atom structures are the active sites during electrolysis [97,98]. Hence, this work highlights the valuable application of electrochemical in situ XAS characterization in understanding the mechanism behind eNO_3RR. Xiao et al. [99] prepared a Cu_6Sn_5 catalyst in another work. They found that the Sn−O signal in Sn K-edge EXAFS spectra and wavelet transform of the k^2-weighted EXAFS spectra gradually weakened and had almost entirely disappeared at -0.2 V vs. RHE (Fig. 6h−j), suggesting the reduction of SnO_x during eNO_3RR in the presence of reactants (NO and H_2O). They also believed that the adsorption of OH* caused the weak Sn−O signal. Meanwhile, the Cu K-edge EXAFS spectra and wavelet transform of the k^2-weighted EXAFS spectra indicate the stable alloy state of Cu during working potentials in eNO_3RR (Fig. 6k−m). Consequently, the insights gained from in situ EXAFS spectra in this work help understand catalysts' chemical state and stability during eNO_3RR. When combined with the in situ XAS results with complementary techniques, like the introduced electrochemical in situ measurements or DFT calculations, electrochemical in situ XAS provides an unprecedented molecular-level view of active site transformations. Although it requires access to synchrotron radiation facilities or X-ray sources capable of providing the necessary energy range and intensity, which may not be readily available, limiting the accessibility of the technique and requiring advanced planning for experiments, XAS measurements continue to reshape the understanding of nitrate conversion pathways and rational catalyst optimization approaches. The ability to correlate metal electronic structures with reactivity in real-time has cemented XAS as an indispensable tool.

Overall, advanced electrochemical in situ characterizations are crucial in exploring new materials and techniques for nitrate reduction. Given the diversity of intermediates involved in nitrate reduction, selecting the appropriate characterization technique is essential to gain a comprehensive understanding of the reaction under different conditions. Table 1 summarizes the advantages, limitations, and applicability of the in situ characterizations introduced in this review.

4. Strategies for eNO₃RR electrocatalyst design

Developing efficient and selective electrocatalysts for eNO_3RR is a key focus area. Optimizing catalysts can enhance their activity, stability, and selectivity toward ammonia production [100]. By discovering new catalyst materials or improving existing ones, researchers can unlock the full potential of eNO_3RR and enable its practical implementation. In eNO_3RR, strategies mainly aim to enhance selectivity and efficiency. Selectivity refers to the ability to selectively produce ammonia without generating undesired by-products. Efficient conversion of nitrate to ammonia is essential to maximize feedstock utilization and minimize energy losses. Strategies that improve selectivity and efficiency can make eNO_3RR economically viable and competitive with traditional ammonia synthesis methods. In this section, we systematically summarize the development of strategies for developing high activity and
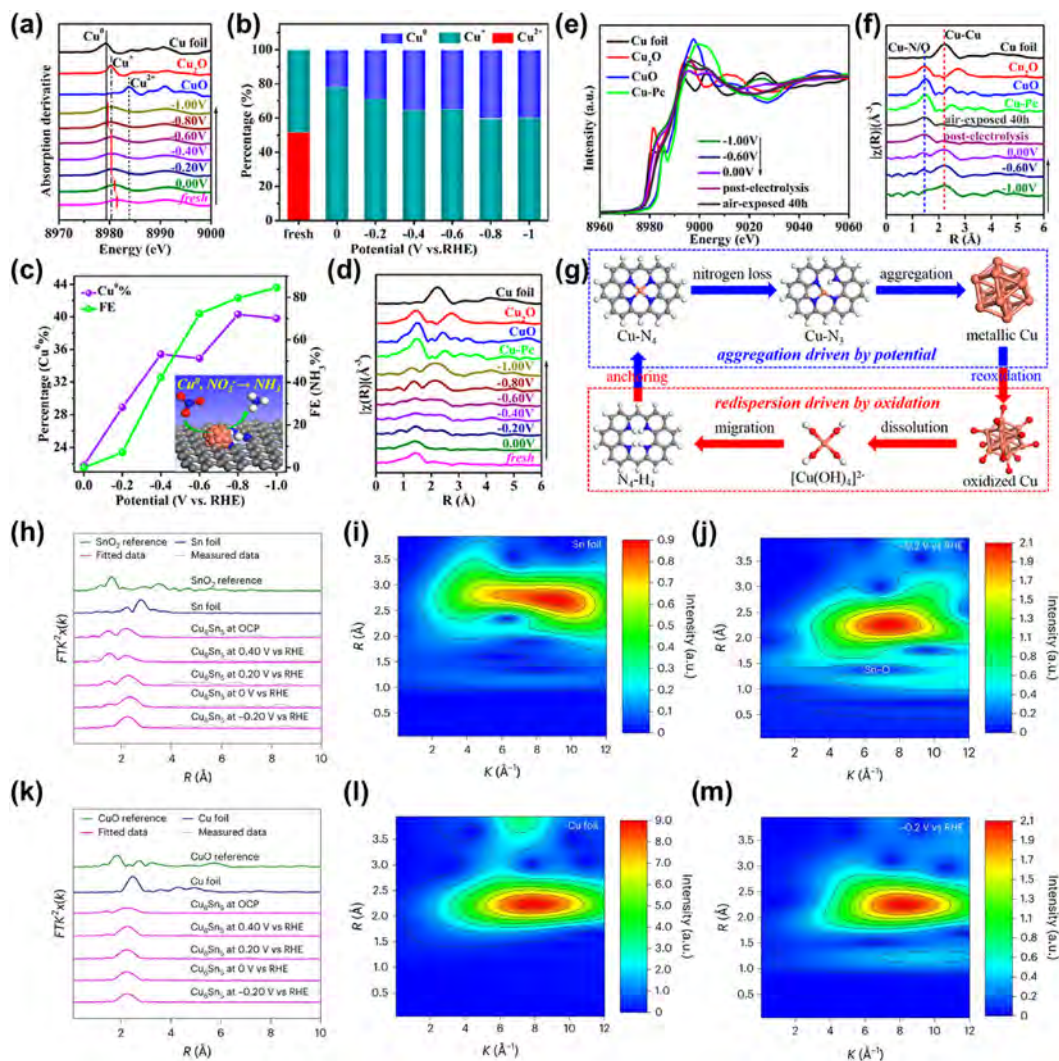
Fig. 6. The application of electrochemical *in situ* XAS measurement in eNO$_3$RR. (a) First-order derivatives of the XANES spectra of Cu−N$_4$ single-atom site collected at different potentials in eNO$_3$RR. (b) Linear combination fitting result of the Cu K-edge XANES spectra in (a). (c) Potential-dependent FE$_{NH3}$ and Cu^0 percentage. (d) Cu K edge FT-EXAFS spectra at different potentials. (e) Cu K-edge XANES spectra and (f) Cu K-edge FT-EXAFS spectra of the samples. (g) Schematic illustration of mechanisms of Cu aggregation driven by the applied potential and redispersion in the oxidation environment. Reproduced with permission [93]. Copyright 2022, American Chemical Society. (h) Sn K-edge EXAFS spectra of the Cu$_6$Sn$_5$ catalyst under different potentials. (i, j) Wavelet transforms of the k^2-weighted EXAFS spectra of Sn foil and Cu$_6$Sn$_5$ at −0.2 V vs. RHE. (k) Cu K-edge EXAFS spectra of the Cu$_6$Sn$_5$ catalyst under different potentials. (l, m) Wavelet transforms of the k^2-weighted EXAFS spectra of Cu foil and Cu$_6$Sn$_5$ at −0.2 V vs. RHE. Reproduced with permission [99]. Copyright 2023, Springer Nature.

selectivity eNO$_3$RR catalysts and reveal the mechanism behind the improved performance.

4.1. Morphology design

Designing catalysts with controlled nanostructures and morphologies can significantly impact eNO$_3$RR performance. It allows for creating high surface area structures, such as nanowires, nanoparticles, or porous architectures [101]. These structures provide a larger active surface area, allowing for more active sites and facilitating enhanced electrochemical reactions. The increased surface area promotes better utilization of the catalyst and improved reaction kinetics. Moreover, tailoring the morphology of electrocatalysts can enhance mass transport properties [102]. Structures with controlled porosity or hierarchical architectures can facilitate the transport of reactants and products, preventing mass transfer limitations and reducing concentration gradients. It also influences the charge transport properties of electrocatalysts. For example, one-dimensional nanostructures like nanowires or nanotubes exhibit faster charge transport due to the facilitated movement of electrons along their length [103]. This promotes efficient electron transfer and minimizes resistive losses within the catalyst, resulting in enhanced reaction kinetics.

Nanomaterial morphology can be divided into zero-dimensional (nanoparticles, atomic clusters), one-dimensional (nanorods, nanowires, nanotubes), two-dimensional (superlattice, ultra-thin film), and three-dimensional (the first three materials are used as basic units) [104]. A graphene nano chainmail-protected iron nanoparticle (Fe@Gnc) electrocatalyst was designed by Yang et al. (Fig. 7a−c) [105]. Because of the high surface and magnetic energy, Fe nanoparticles easily aggregate and thus lead to lower active site exposure. Also, it is reported that Fe-based nanocatalysts could only maintain 5~10 electrochemical cycles due to poor long-term durability and low kinetic stability [106,107]. The authors ingeniously synthesized an ultrathin graphene nanosheet outside the Fe nanoparticles via a simple hydrothermal method and *in situ* thermal reduction strategy, protecting the active sites and suppressing the oxidation and leakage of Fe nanoparticles. Such graphene

Table 1
Summary of the advantages, limitations, and applicability of the different *in situ* characterization techniques.

Electrochemical *in situ* characterizations	Advantages	limitations	Applicability
DEMS	1. It allows for the simultaneous measurement and identification of gas-phase products like NO_2, NO, and NH_3. 2. It enables quantitative analysis of the gas-phase products. 3. It allows for the identification of short-lived species in electrochemical reactions.	1. The sensitivity of DEMS measurements may vary depending on the mass spectrometer used, potentially limiting the detection of certain low-abundance species or isotopes. 2. It is limited to gaseous reaction products. It may not be suitable for detecting or quantifying non-volatile or semi-volatile species that cannot reach the gas-phase. It may not be efficiently ionized and detected by the mass spectrometer.	It can provide online signals for volatile intermediates/products.
FTIR	1. It allows for real-time and non-destructive analysis of the reaction mixture. 2. It provides molecular-level information about the functional groups during the reaction. 3. It allows for the study of nitrate reduction under realistic conditions.	1. A suitable IR-transparent window material is required to withstand the reaction conditions. 2. The weak vibration mode or low concentration of some reaction products or intermediates makes their detection and characterization challenging. 3. FTIR spectra can exhibit a wide range of peaks due to the presence of different molecular species, functional groups, and background interference.	It provides valuable molecular-level insights into the reaction intermediates and mechanisms of eNO$_3$RR under working conditions.
ESR	1. It allows for the real-time monitoring of the formation and decay of DMPO radical adducts during the eNO$_3$RR. 2. It can provide quantitative information about the concentration of paramagnetic species.	It is not suitable for the electron-mediated pathway in eNO$_3$RR.	It is beneficial for studying hydrogen radicals in eNO$_3$RR.
Raman	1. It provides real-time molecular-specific information on reaction intermediates, products, and adsorbed species during the eNO$_3$RR. 2. It is a non-destructive and non-invasive technique that can be performed under ambient conditions. 3. Electrochemical surface-enhanced Raman spectroscopy (SHINERS) allows for *in situ* characterization and analysis of electrochemical processes and detecting trace-level analytes with high sensitivity. 4. It provides valuable information about materials' physical properties and structural changes.	1. It is susceptible to fluorescence interference. 2. Multiple species contribute to the observed signals that may cause spectral overlapping. 3. The spatial resolution of Raman spectroscopy is limited by diffraction, typically in the range of micrometers.	It is a valuable tool for studying chemical reactions, materials transformations, and structural changes in real-time and provides molecular-scale details in eNO$_3$RR.
XAS	1. It provides real-time element-specific structural and electronic information about the species involved in nitrate reduction, such as the oxidation state, coordination environment, and local structure. 2. It is susceptible and can detect species at low concentrations or in complex mixtures. 3. It can provide quantitative information about the concentration and oxidation state of elements, facilitating the analysis of reaction kinetics, and determining reaction mechanisms.	1. The synchrotron radiation facilities or X-ray sources may not be readily available. 2. It has limited time resolution, which may restrict the ability to capture fast kinetics or transient intermediates during nitrate reduction. 3. The analysis of XAS data involves complex data analysis techniques and the use of reference standards.	It can directly probe the catalytic active sites and analyze the local geometric and electronic structure.

nanochainmail strategy allows Fe@Gnc to maintain a long-term high nitrate removal rate. Furthermore, Xi et al. constructed a Bi−Co corridor-like structure by depositing Co at the bottom and utilizing the limited electron accessibility of Bi element [108]. Based on the scanning electron microscope (SEM) and transmission electron microscopy (TEM) images (Fig. 7d and e), the Co+Bi@Cu nanowire has a three-dimensional structure of Bi−Co corridor with Bi nanoparticles in the outer layer and Co hexagonal sheets in the inner layer. The results revealed that Co sites at the bottom could easily adsorb NO_3^-, while the outer Bi could trap the escaped NO_2^- and
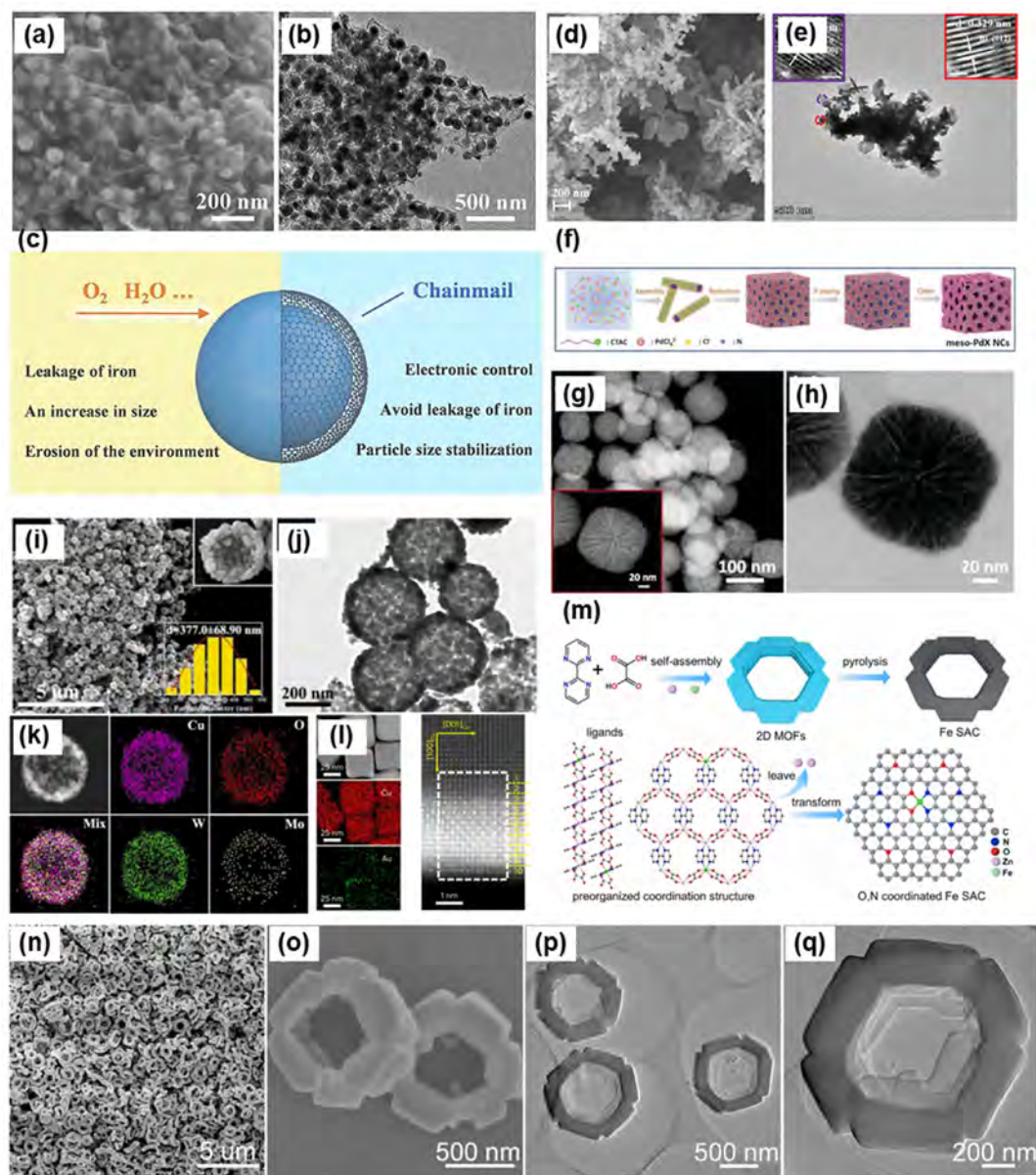
Fig. 7. Morphology design of catalysts in eNO$_3$RR. (a) SEM image, (b) HRTEM image, and (c) schematic illustration of the role of graphene nanochainmail for the Fe@Gnc sample. Reproduced with permission [105]. Copyright 2023, John Wiley and Sons. (d) SEM image and (e) TEM images of Co+Bi@Cu NW. Reproduced with permission [108]. Copyright 2023, John Wiley and Sons. (f) Schematic illustrations of the preparation process, (g) HAADF STEM image, and (h) TEM image of binary meso-PdX NCs. Reproduced with permission [113]. Copyright 2023, John Wiley and Sons. (i) SEM image, (j) TEM image, and (k) the corresponding TEM-EDS elemental mapping images of Mo/H−CuW. Reproduced with permission [116]. Copyright 2022, Elsevier. (l) HAADF-STEM image and corresponding elemental mapping of Cu/CuAu alloy nanocubes. Reproduced with permission [118]. Copyright 2023, Springer Nature. (m) Schematic illustration of the synthetic process of the Fe single-atom catalysts (SAC). (n, o) SEM images and (p, q) TEM images of bimetallic (FeZn) MOF. Reproduced with permission [119]. Copyright 2022, Elsevier.

reduce them into NH$_3$, achieving an FE$_{NH3}$ of nearly 100%. Furthermore, the engineering of crystalline mesoporosity at the mesoscopic level has emerged as a promising strategy to enhance the selectivity of multistep reactions [109,110]. Concave/convex surfaces, characteristic of crystalline mesoporous materials, provide a higher density of catalytically active sites, enhancing the reactivity toward specific desired products [111,112]. Liu et al. [113] prepared a series of mesoporous PdX nanocubes (meso-PdX NCs, X represents metal−non-metal) as electrocatalysts for selective eNO$_3$RR to NH$_3$. In the schematic illustrations of preparing binary meso-PdX NCs (Fig. 7f), meso-Pd NCs were firstly prepared in the environment of assembled cylinder micelles of cetyltrimethylammonium chloride and capping agent of Cl$^-$, and then introducing non-metal (X) into Pd

nanocrystals through an *in situ* doping route. It could be seen that the highly uniform and homogeneously dispersed macroscopic NC morphology in Fig. 7g and h, as well as abundant penetrated mesopores, extended radially from the center of the NC. The synergistic effect between the unique macroscopic NC morphology, abundant mesoscopic mesoporous structure, and the uniform non-metal alloy contribute to superior eNO$_3$RR performance. The as-prepared catalyst had the highest FE$_{NH3}$ of 96.1% and NH$_3$ yield rate of 3760.4 μg/h/mg$_{cat}$. Besides the research around 0D, 1D, and 2D nanostructures, many state-of-the-art electrocatalysts are designed within 3D nanostructures or multidimensional composite structures [114]. Compared with low-dimensional structures, the interconnected network or porous nature in 3D or multidimensional structures

facilitates the diffusion of molecules, ions, and electrons within the structure. This promotes faster reaction kinetics and minimizes diffusion limitations, improving performance [115]. Also, the spatial arrangement and interaction between different components can result in synergistic effects. The synergistic effects arise from the efficient coupling of active sites and optimized charge transfer pathways. In our previous work, we reported copper tungstate ($CuWO_4$) hollow nanospheres with Mo clusters and high concentration of asymmetric oxygen vacancies (denoted as Mo/H−CuW) for highly efficient eNO$_3$RR (Fig. 7i−k) [116]. The morphology of $CuWO_4$ was observed to be affected by the duration of the hydrothermal process. As the duration increased from 6 h to 48 h, the size of the nanospheres exhibited a progressive increase from approximately 305 nm to around 372 nm. Additionally, the nanospheres underwent three distinct transformations: solid nanospheres, hollow nanospheres, and ultimately, fragmented spheres. The hollow structure offers a larger specific surface area, exposing more active sites and promoting. 3D structures also offer more design flexibility compared to 2D or 1D structures [117]. The arrangement of materials in three dimensions allows for precise control over the active sites' composition, morphology, and spatial distribution. For example, Zhu et al. [118] designed core/shell nanocrystals (NCs) of Cu/CuAu by direct solution-phase synthesis (Fig. 7l). The gold atoms are found to be uniformly dispersed on the surface of the nanocubes, while the copper atoms are observed to be spread throughout the entire structure, aligning with the particle morphology characterized by an intermetallic CuAu shell encompassing a copper core. The catalysts exhibit remarkable selectivity toward NH$_3$ in eNO$_3$RR, achieving an impressive faradaic efficiency of 85.5% at −0.5 V vs. RHE. The enhanced performance is because of {001}-oriented copper site ensembles, which optimized the chemisorption toward *NO$_3$ and *N. It strengthens the binding of *NO$_3$ species by causing an upshift in the d-band center of the surface copper atoms. It weakens the *N anchoring due to strong repulsive interactions from a subsurface gold ligand or surface gold single atom. In the work from Gu et al. [119], they prepared N, O co-coordinated MOF structure with a nut-like morphology that exhibited high faradaic efficiency (~92%) and high ammonia yield rate (46 mg/h/mg$_{cat}$) in neutral electrolytes. In the preparation process, Zn and Fe ions with 2,2′-bipyrimidine and oxalic acid ligands formed N, O co-coordinated structure through self-assembly, followed by one-step pyrolysis to synthesize porous carbon supported Fe single-atom catalysts (Fe SACs, Fig. 7m). The SEM and TEM images of bimetallic (FeZn) MOF reveal a distinct nut-like morphology. This nut-like structure is formed by assembling six cuboids with an outer diameter of 1250 nm and an inner diameter of 782 nm. Moreover, upon closer examination, an intrinsic 2D-layered structure can be observed at the inner edge of each MOF nut. This layered structure likely arises from the arrangement of the MOF's constituent atoms or molecules in a stacked fashion, leading to a distinct layered morphology within the nut-like structure (Fig. 7n−q).

In summary, morphology design in eNO$_3$RR offers tremendous opportunities to optimize catalytic performance. By tailoring the morphology of electrocatalysts, it is possible to enhance the active surface area, improve mass and charge transport, tune catalytic sites, and leverage synergistic effects. These advancements contribute to developing efficient and selective electrocatalysts for various electrochemical reduction reactions, enabling sustainable energy conversion and storage technologies.

4.2. Alloying engineering

As researchers seek to develop highly efficient and durable nitrate reduction catalysts, alloying different metals has emerged as a powerful design approach. This approach involves the design and synthesis of bimetallic or multimetallic catalysts with specific alloy compositions to enhance the catalytic activity, selectivity, and overall performance in nitrate reduction reactions [120]. The most significant advantage of alloying engineering is the synergistic effects, where the combined properties of the individual metals result in enhanced catalytic activity [121]. The alloying process can create unique active sites, modify the electronic structure, and optimize the adsorption and activation of reactants, thereby improving the eNO$_3$RR performance.

Among the metals reported in the application of eNO$_3$RR, Cu represents a highly efficient cathode electrocatalyst, and various Cu-based catalysts have recently been investigated [122−126]. To address the problems of the high overpotential for driven eNO$_3$RR and aggregated NO$_2^-$ in the electrolyte, alloying Cu with other metals has been employed to improve the intrinsic activity of Cu [60,98]. Take gold as an example; the Cu/CuAu ordered single-atom alloy nanocubes prepared directly in the solution-phase without solid-state thermal treatment show stronger *NO$_3$ binding and weaker *N binding than Cu (100) (Fig. 8a−c) [118]. The alloyed CuAu adjusted the electronic structures and led to an increased d-band center of copper atoms for the CuAu surface compared with other surfaces, leading to a stronger binding of *NO$_3$. Simultaneously, the subsurface gold in the catalytic system interacts primarily in a repulsive manner due to its fully occupied d-band and large d-orbital radius. The repulsive interaction between the subsurface gold and nitrogen-bonded species contributes to the observed facile removal of these species during the catalytic process. This CuAu alloy system showed a high selectivity toward NH$_3$ from the electrocatalytic nitrate reduction reaction. Due to their abundance and natural roles in nitrogen transformations, late-transition metals like cobalt, nickel, and iron are attractive alloy partners [127]. Alloys pairing noble metals with these have exhibited synergistic promotional effects through electronic interactions. Sun et al. reported CuCo alloy nanosheets to mimic the behavior of the two catalytic centers in Cu-NIRs [58,128]. The Cu$_{50}$Co$_{50}$ alloy exhibits the highest current density of NH$_3$ and FE compared with monometallic Cu and monometallic Co catalysts (Fig. 8d and e). Through DFT calculations, the Co species could efficiently balance the adsorption energy between *H and *NO$_3$ species. The synergy between Cu and Co can reduce the high energy barrier in eNO$_3$RR and make the *H preferentially adsorbed on the Co surface to avoid excessive *H occupation of the active sites (Fig. 8f and g). The enhanced eNO$_3$RR activity can also be observed by doping ruthenium (Ru) into Cu, where Fig. 8h shows the yield rate of NH$_3$ enhanced with the increase of the Ru/Cu molar ratio from 0.06 to 1 [85]. The turnover frequency (TOF) results demonstrate the markedly synergetic effect of Ru and Cu, in which the Cu promotes the conversion from NO$_3^-$ to NO$_2^-$ while Ru exhibits the superior activity for NO$_2^-$ to NH$_3$ (Fig. 8i). Similar works are reported about alloy Cu with Pd and Ni [129,130], in which Pd alloying could act as active sites for adsorption of H-atoms, thus promoting the hydrogenation of eNO$_3$RR (Fig. 8j). In the meantime, both Ni and Pd could tune the d-band center of Cu, which leads to a modulation of intermediates adsorption during eNO$_3$RR (Fig. 8k). Besides the excellent Cu cathode, other alloys, such as RuFe bimetallic alloy [131], also attract much interest from researchers. The RuFe bimetal alloy loaded on nitrogen-doped carbon with a single Fe atom (RuFe−FeNC) ranks at the top of the state-of-the-art in the report from Yan et al. (Fig. 8l). The RuFe−FeNC catalysts have a higher selectivity to NH$_3$ than other by-products and show excellent stability (Fig. 8m and n).

Therefore, alloying engineering presents a pathway to design bimetallic or multimetallic catalysts with enhanced catalytic activity and selectivity. Combining different metals in alloys can result in synergistic effects, where the overall catalytic performance
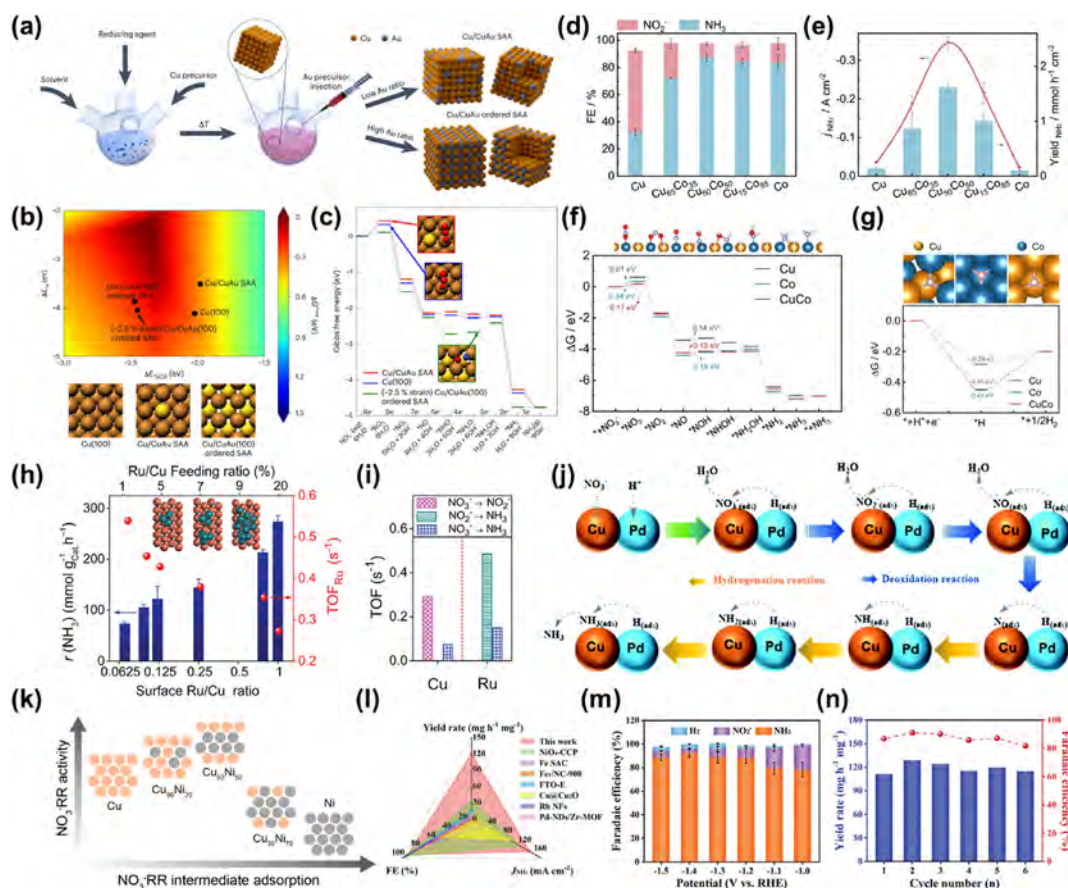
Fig. 8. Alloying engineering of catalysts in eNO₃RR. (a) Schematic illustration of the core/shell Cu/CuAu SAA synthesis. (b) Activity volcano plot using the binding energies of *NO₃ and *N as descriptors. (c) Gibbs free energies for different intermediates over Cu(100), strained ordered Cu/CuAu(100) SAA, and Cu/CuAu SAA. Reproduced with permission [118]. Copyright 2023, Springer Nature. (d) FE of NH₃ and NO₂⁻, and (e) current density and products yield for NH₃ of the samples. (f, g) Gibbs free energies for different intermediates in eNO₃RR and HER at −0.2 V vs. RHE on CuCo (111), pure Cu (111), and pure Co (111) surfaces, respectively. Reproduced with permission [58]. Copyright 2022, Springer Nature. (h) The catalyst mass-normalized yield for NH₃ and turnover frequency (TOF_Ru, after deducting surface-exposed Cu contribution) for eNO₃RR of Ru_x/Cu₁₀/rGO. The inset shows the catalyst model: golden and dark green spheres represent Cu and Ru atoms, respectively. (i) The TOF of Ru/rGO and Cu/rGO for converting NO₃⁻/NO₂⁻ to NH₃. Reproduced with permission [85]. Copyright 2023, John Wiley and Sons. (j) Schematic illustration showing the eNO₃RR mechanism over CuPd alloy. Reproduced with permission [129]. Copyright 2021, Royal Society of Chemistry. (k) The relation between eNO₃RR activity and intermediates adsorption on different CuNi alloys. Reproduced with permission [130]. Copyright 2020, American Chemical Society. (l) Performance comparison of RuFe−FeNC with other reported electrocatalysts. (m) FE of different products of RuFe−FeNC obtained in 0.5 M K₂SO₄ + 0.1 M KNO₃. (n) eNO₃RR activity of RuFe−FeNC in durability test at −1.4 V vs. RHE. Reproduced with permission [131]. Copyright 2023, John Wiley and Sons.

is significantly enhanced compared to individual metal components. Synergies can arise from alloy-induced electronic interactions, lattice strain effects, or modified surface chemistry. These synergistic effects can improve the catalytic activity, selectivity, and stability in eNO₃RR. The systematic investigation of alloy compositions and their structure-property relationships offers valuable insights into the underlying mechanisms. It can guide the development of highly efficient catalysts for nitrate reduction applications.

4.3. Defect engineering

While alloying focuses on optimizing electronic structure through compositional tuning, defect engineering provides another handle to tailor catalyst properties. Defect sites, including vacancies, interstitials, and irregular coordination environments, can strongly influence adsorption behavior [132].

Among various defect types, oxygen vacancies on metal oxide catalysts have attracted significant interest for eNO₃RR due to their ability to tune the electronic properties and surface adsorption behavior. Taking the cation substitution strategy, abundant oxygen vacancies were introduced into LaFeO₃₋δ (LF) by replacing the Fe site with metal element M (M = Co, Ni, and Cu) to form

LaFe₀.₉M₀.₁O₃₋δ perovskite submicrofbers [133]. Combined with the results of KPFM and COMSOL multiphysics simulations, the results indicate LaFe₀.₉M₀.₁O₃₋δ has a higher surface potential and work function than that of LF, which means a more minor energy barrier for electron transfer to the NO₃⁻ and induces NO₃⁻ enrichment than H⁺ (Fig. 9a−f). Sun et al. [134] also reported defective Fe₂TiO₅ in eNO₃RR. The generated oxygen vacancy due to the Fe element having high reducibility of randomly displacing Ti⁴⁺ could enhance conductivity and cause an extremely low free energy (−0.28 eV) of nitrate adsorption (Fig. 9g) [135]. Constructing surface metal atomic vacancies has recently been another effective defect engineering method for promoting eNO₃RR properties. For example, Cu vacancies were introduced into Au₁Cu single-atom alloys (V_Cu−Au₁Cu SAAs) via a facile galvanic replacement with a subsequent dealloying process (Fig. 9h), which regulates the local electronic and geometric structure with the help of Au single-atom, showing an FE_NH3 of 98.7% with a yield rate of 555 μg/h/cm at −0.2 V vs. RHE (Fig. 9i−k) [136]. Therefore, combining defects with other catalytic strategies, such as alloying or surface modifications, can result in synergistic effects that further enhance the performance of catalysts in eNO₃RR. The interaction between defects and other catalytic features can create cooperative effects, improving catalytic activity, selectivity, and stability. Doping is

another effective defect strategy to tune the catalytic properties. Experimental studies found that interstitial C dopant in Co_3O_4 could induce a local electric field and thus efficiently facilitate the conversion from NO_2^- to NH_3, which exhibits an FE of nearly 100% for NH_3 production in a wide potential window from -0.1 V to -0.6 V vs. RHE (Fig. 9l and m) [137]. The faster nitrite reduction to ammonia has a valuable guiding significance for eNO_3RR. Besides the vacancies and doping defects, grain boundaries (GBs) represent a particular defect within polycrystalline metal and oxide catalyst materials [138]. As interfaces between misoriented crystalline grains, GBs disrupt the periodic lattice and generate locally distorted coordination environments. Fu and his coworkers proposed a GB defect engineering in Ni nanoparticles to trap *H from quickly releasing hydrogen to form hydrogen [139]. The presence of abundant GBs not only regulates the *H adsorption but also promotes the rate-determining step of NO_3^* to NO_2^* in eNO_3RR, thus achieving a high FE_{NH3} of 93.0% and yield rate of 15.49 mmol/h/cm^2 (Fig. 9n−q). Lattice strain is also essential when intentionally

engineering defects into catalyst materials. Distorting bond angles and lengths near defect sites can strongly influence local adsorption and catalytic properties [140]. In our previous work, we took advantage of the strong interaction of Pt−Ce pairs to successfully tailor the interlayer spacing of 2D SnS nanosheets, including both expansion and compression [82]. The doped Pt and Ce elements contribute to the expansion of interlayer spacing from 5.672 ± 0.019 Å to 6.040 ± 0.034 Å and shrinkage from 5.898 ± 0.028 Å to 5.220 ± 0.031 Å) (Fig. 9r and s). Interestingly, the DFT results indicate that smaller spacings intensify the delocalization of p electrons in Sn-5p orbitals, resulting in an increased chemical affinity toward NO_3^- and NO_2^- while concurrently inhibiting hydrogen generation (Fig. 9t−v). Consequently, the designed Pt-intercalated Ce-doped SnS ($Pt_{0.9}/Ce_{0.5}$-SS) shows a good FE_{NH3} (94.12%) and yield rate (0.3056 mmol/cm^2/h).

Overall, defect engineering offers a powerful approach to tailor the eNO_3RR activity. By introducing or manipulating defects, it is possible to enhance activity and selectivity in eNO_3RR significantly.
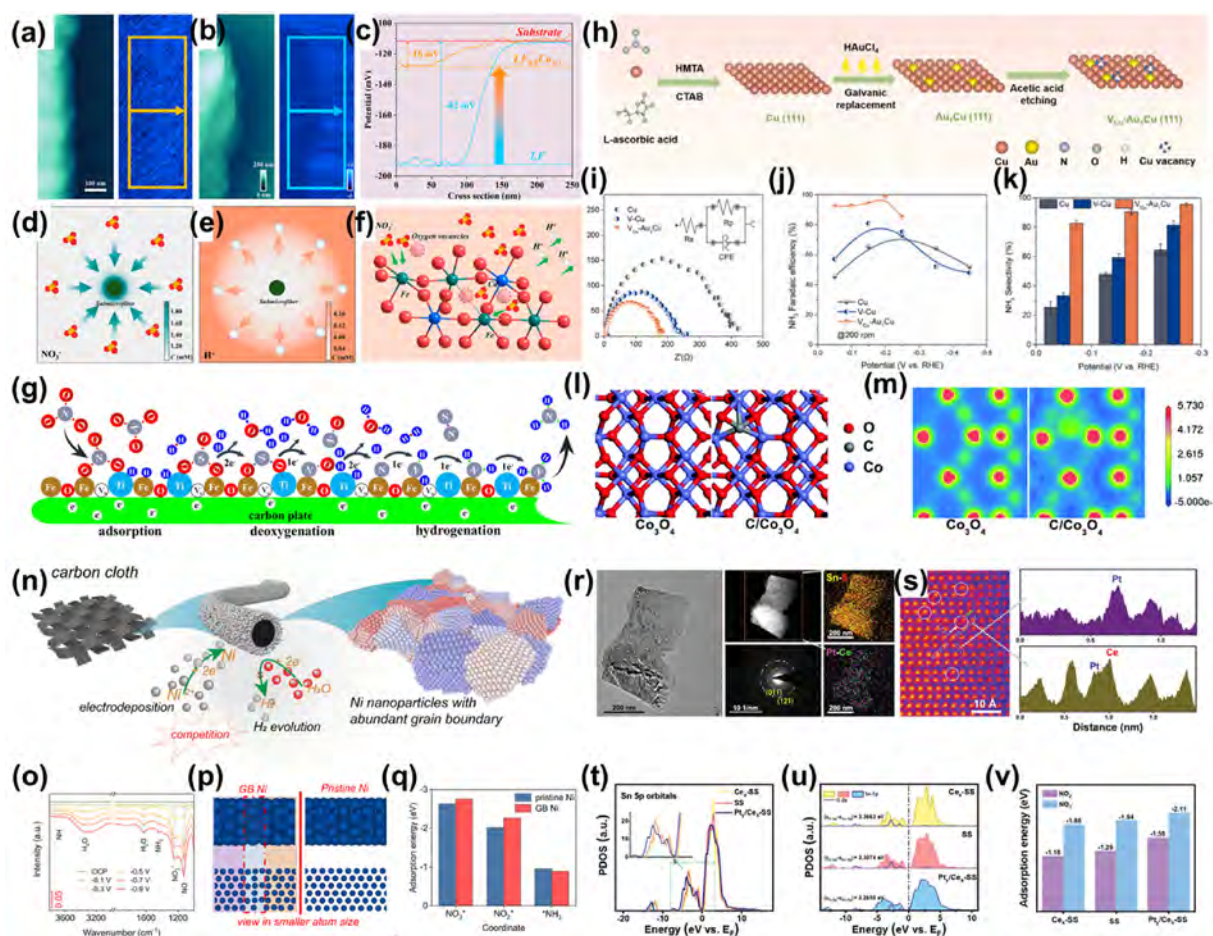
Fig. 9. Defect engineering of catalysts in eNO_3RR. (a, b) Surface potential distribution of $LF_{0.9}Cu_{0.1}$ and LF submicrofbers. (c) The extracted surface potential values from (a, b). (d, e) Top view of the variation model of NO_3^- and H^+ concentrations on the fiber surface. (f) Schematic illustration of the ion movement on the catalyst surface with more positive potential. Reproduced with permission [133]. Copyright 2023, American Chemical Society. (g) Pathway for eNO_3RR over the Fe_2TiO_5 nanofiber. Reproduced with permission [134]. Copyright 2022, John Wiley and Sons. (h) Schematic diagram of the V_{Cu}−Au_1Cu SAAs synthesis. (i) Nyquist plots, (j) FE_{NH3} and (k) selectivity of NH_3 over various samples. Reproduced with permission [136]. Copyright 2022, Elsevier. (l) Optimized Co_3O_4 and C/Co_3O_4 structures along the (311) plane. (m) The corresponding electron contour maps of the (311) slice in (l). Reproduced with permission [137]. Copyright 2022, Royal Society of Chemistry. (n) Schematic diagram of GB defect-engineered Ni NPs synthesis. (o) *In situ* ATR-FTIR spectra of different intermediates in eNO_3RR. (p) The built structure model of GB Ni and pristine Ni for DFT calculations. (q) Adsorption energy of the three key species on GB Ni and pristine Ni. Reproduced with permission [138]. Copyright 2023, Royal Society of Chemistry. (r) TEM, STEM image, corresponding EDX mappings, and SAED pattern of $Pt_{0.9}/Ce_{0.5}$-SS. (s) HAADF-STEM image of $Pt_{0.9}/Ce_{0.5}$-SS and the corresponding line intensity profiles in the selected regions marked by the gray dashed line. The green and white arrows point to the Ce and Pt atoms, respectively. (t) The PDOS diagrams of Sn-5p orbitals. (u) The PDOS diagrams of Sn-5p and O-2p orbital for NO_3^- adsorbed on the models. (v) Adsorption energies of NO_3^- and NO_2^-. Reproduced with permission [82]. Copyright 2023, John Wiley and Sons.

The synergistic effects of defects with other catalytic strategies further expand the potential of defect engineering in advancing eNO₃RR and contributing to sustainable nitrogen cycle management.

4.4. Heterostructures

Heterostructures, composite materials composed of two or more distinct components with different properties, have gained considerable attention in nitrate reduction due to their unique structural and functional advantages [141]. By combining materials with tunable electronic structures and reactive sites, heterostructures open unprecedented opportunities to tailor functionality. The critical advantage of heterostructures is the synergistic catalytic activity, which combines the favorable properties of different components. The interface between the two materials in a heterostructure can promote charge transfer, modify the electronic structure, and enhance the adsorption and activation of nitrate species [142,143]. Early studies coupling metals to metal oxides found synergistic promotion effects exceeding monolithic counterparts. A heterostructured electrocatalyst was created by coupling CuCl (111) and rutile TiO₂ (110) [144]. As

shown in Fig. 10a, a built-in electric field was formed in the interface of TiO₂/CuCl (CuCl_BEF), leading to the electron transfer. The authors utilized molecule dynamics to simulate the liquid status. It could be observed that the maximum concentration of NO_3^- close to the side of CuCl_BEF is higher than that on pure CuCl surface (Fig. 10b and c). The finite element analysis also revealed an accumulation of 140 mg/L of NO_3^- near the junction after 0.1 ns due to the built-in electric field. In contrast, pure CuCl did not exhibit this effect (Fig. 10d). In another work, Schuhmann et al. [145] presented a design for the electrochemical transformation of CuCo binary sulfides into potential-dependent core-shell Cu/CuOₓ and Co/CoO phases (Fig. 10e and f). The inner Cu/CuOₓ and Co/CoO heterostructures catalyze to converse NO_3^- to NO_2^- and NH₃, respectively. This unique tandem catalyst system leads to an FE_NH3 of 93.3 ± 2.1% and a high NH₃ yield rate of 1.17 mmol/cm²/h in 0.1 M NO_3^- at −0.175 V vs. RHE.

Therefore, heterostructures are a promising design strategy for nitrate reduction catalysts. Their intricately tunable multi-phase interfaces hold tremendous promise to address the grand challenge of selectively producing value-added nitrogen products.
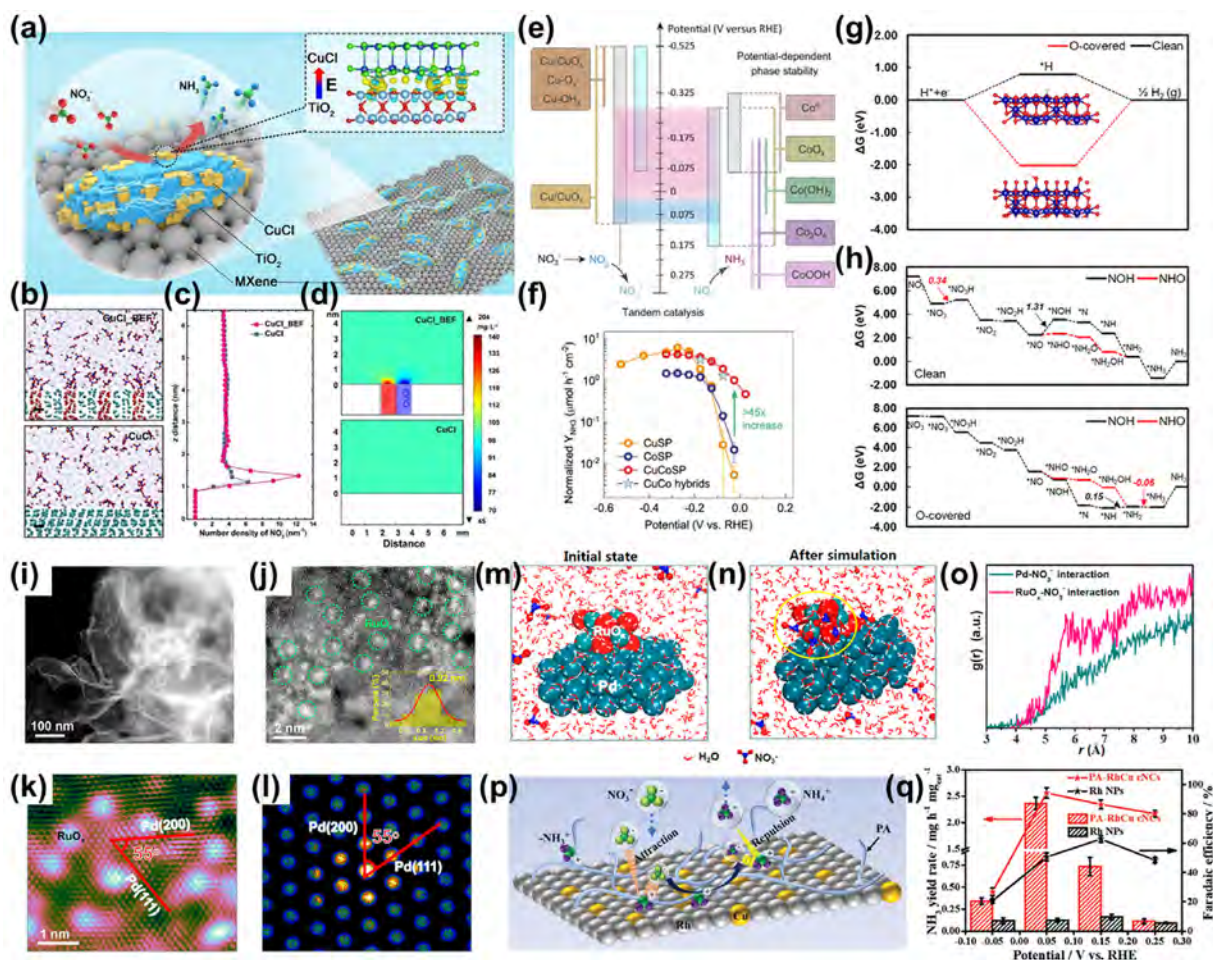
Fig. 10. Heterostructures and surface functionalization design of the catalysts in eNO₃RR. (a) Illustration of the CuCl_BEF on the MXene surface. (b) Molecular dynamics simulation of CuCl and CuCl_BEF in 100 ppm KNO₃. Scale bar, 0.5 nm. (c) Distribution of NO_3^- along the z-axis electrode distance based on (b). (d) Finite element analysis of ions distribution difference near CuCl and CuCl_BEF in KNO₃ solution. Reproduced with permission [144]. Copyright 2021, John Wiley and Sons. (e) The potential range for tandem reduction of NO_3^- to NH₃. (f) The ECSA-normalized yield of NH₃ in 0.01 M NO_3^- + 0.1 M KOH. Reproduced with permission [145]. Copyright 2022, Springer Nature. (g, h) Gibbs free energy diagram for HER and eNO₃RR. Reproduced with permission [150]. Copyright 2021, American Chemical Society. (i) HAADF-TEM image, (j) aberration-corrected HAADF-STEM image (inset: cluster size distribution), (k) IFFT, and (l) FFT image of RuOₓ/Pd. (m, n) Snapshots for the dynamic process of NO_3^- adsorption on RuOₓ/Pd before and after molecule dynamics simulations and corresponding (o) RDF curves of Pd−NO_3^- and RuOₓ−NO_3^- interactions. Reproduced with permission [70]. Copyright 2023, American Chemical Society. (p) Schematic diagram of PA-induced enhanced interfacial mass transfer process by the electrostatic interaction during eNO₃RR. (q) FE and yield of NH₃. Reproduced with permission [152]. Copyright 2022, John Wiley and Sons.

4.5. Surface functionalization

Tailoring the catalyst surface through functionalization or modification can improve its catalytic activity and selectivity. Techniques like electrodeposition, atomic layer deposition, and surface ligand exchange can introduce desired functionalities, control catalyst morphology, and enhance catalytic performance [146].

Negatively charged species, such as chloride anions on surfaces, are reported to capture protons, limiting the hydrogen evolution reaction, and enhancing the selectivity of cathodic reductions [147−149]. Utilizing this surface modulation strategy to create advanced eNO$_3$RR catalysts, shows promise. Consequently, researchers synthesized ultrathin CoO$_x$ nanosheets with abundant adsorbed oxygen on the surface to modulate the eNO$_3$RR performance [150]. The higher free energy of *H adsorption of O-covered CoO$_x$ than clean CoO$_x$ indicates the stronger interaction between *H and the O-covered surface and suppressed HER, as shown in Fig. 10g. In the meantime, CoO$_x$ with an oxygen-modified surface could also lower the energy barriers to producing ammonia (Fig. 10h). Chu et al. [70] found that the sub-nm RuO$_x$ clusters anchored on a Pd metallene (RuO$_x$/Pd) serve as a highly effective eNO$_3$RR catalyst. As shown in the HAADF-TEM and STEM images (Fig. 10i and j), the numerous subnanometer clusters with a size of ~0.92 nm were distributed on the graphene-like Pd metallene. From the inverse fast Fourier transform (IFFT, Fig. 10k) and fast Fourier transform (FFT, Fig. 10l) analyses, they showed that the lattice fringes and diffraction spots observed in RuO$_x$/Pd which can all be attributed to Pd crystal structures, specifically Pd (111) and Pd (200) with a crossing angle of 55° [151]. No crystalline features of RuO$_2$ were detected, indicating that RuO$_x$ clusters with sub-nanometer size are epitaxially grown on the Pd metallene, ruling out the formation of RuO$_2$. They also found a higher NO$_3^-$-coverage on RuO$_x$/Pd than on Pd substrate and the corresponding higher radial distribution function (RDF) of NO$_3^-$-RuO$_x$ interaction than NO$_3^-$-Pd interaction (Fig. 10m−o). In another work, Chen et al. [152] suggested a design of polyallylamine (PA)-functionalized frame-like concave RhCu bimetallic nanocubes (PA-RhCu cNCs). Upon the PA functional molecule, PA-RhCu cNCs show a higher electrochemically active surface area (72.8 m^2/g) than Rh NPs. Positively charged PA-Rh cNCs attract negatively charged NO$_3^-$ ions through electrostatic attraction, enriching NO$_3^-$ ions at the electrode/solution interface. Additionally, PA-Rh cNCs with −NH$_3^+$ groups efficiently repel NH$_4^+$ ions formed on the Rh surface due to electrostatic repulsion, which aids in the mass transfer of products (Fig. 10p). The system exhibits a FE$_{NH3}$ of 93.7% with a high yield rate of 2.40 mg/h/mg$_{cat}$ (Fig. 10q).

In summary, functionalizing surfaces through atomic-scale engineering of surface terminations and anchored complexes present exciting avenues to optimize eNO$_3$RR catalysts. With further exploration, it could yield new materials surpassing conventional bulk-oriented designs.

5. Summary and outlook

Electrochemical nitrate reduction is rapidly gaining significance in nitrogen cycle management, agriculture, and environmental remediation. It is emerging as a promising pathway for the production of green ammonia. Consequently, acquiring a comprehensive understanding of the reaction mechanism and developing electrocatalysts with superior activity and faradaic efficiency is paramount. This review encapsulates the latest developments in understanding the nitrate reduction mechanism and the rational strategies for catalyst design. *In situ* characterization studies have been instrumental in shedding light on reaction intermediates and

pathways, thereby guiding the design of catalysts with enhanced activity and selectivity. Specifically, we delve into various innovative approaches employed to optimize catalyst performance, such as alloying, defect engineering, and surface functionalization. While advanced materials boasting high activity, selectivity, and stability have been developed, the journey toward realizing industry-scale applications is still ongoing, with several unresolved issues warranting attention. The following descriptions provide a detailed exploration of these aspects:

1) Although more and more *in situ* electrochemical measurements are developed to study the reaction mechanism of eNO$_3$RR, the nitrate reduction reaction involves multiple steps and intermediates, making it challenging to identify and characterize each species. *In situ* measurements often require high sensitivity to detect and identify low-concentration intermediates and reaction products. The limited concentration of these species, combined with potential interference from background signals or other electrochemical processes, can hinder accurate detection and characterization. Therefore, selecting the appropriate *in situ* measurement techniques that can provide relevant information about the reaction mechanism is crucial. Different approaches have limitations and strengths, and it is essential to choose complementary methods to address the specific challenges associated with nitrate reduction. Overcoming these challenges requires combining electrochemistry, spectroscopy, and data analysis expertise. It often involves the development of advanced experimental set-ups, using state-of-the-art instrumentation, and integrating complementary techniques to obtain a more comprehensive understanding of the eNO$_3$RR mechanism.

2) The surface of the catalyst undergoes dynamic changes during eNO$_3$RR. Adsorption and desorption of reaction intermediates can induce surface reconstruction, resulting in modifications to the active sites and surface morphology. Capturing and comprehending these dynamic changes in real-time poses significant challenges. Surface reconstruction during nitrate reduction can involve changes in surface composition, crystallographic orientation, and atomic arrangement. Therefore, using advanced characterization techniques with exceptional spatial resolution and sensitivity is essential. Meanwhile, surface reconstruction processes can be influenced by reaction time and temperature. Different reaction conditions can lead to variations in reconstruction dynamics, making it crucial to carefully control and characterize these parameters to assess surface changes accurately.

3) It is required to set standardized criteria for assessing eNO$_3$RR performance. The absence of standardized criteria makes it challenging to compare the effectiveness of different catalysts. Without uniform metrics or protocols, researchers may use different performance indicators, such as current density, selectivity, or energy efficiency, making it difficult to draw meaningful conclusions or establish direct comparisons between catalysts. Additionally, variations in experimental setups, electrode materials, and testing conditions can further contribute to inconsistencies in reported performance. Standardized criteria would facilitate more accurate and reliable comparisons, enabling a better understanding of catalyst performance and the identification of promising materials for eNO$_3$RR.

4) Controlling and optimizing reaction conditions are the way to achieve reproducibility and relevance to practical applications. The choice of reaction conditions, including pH, temperature, and electrolyte composition, can significantly influence the eNO$_3$RR mechanism and the formation of intermediates.

However, determining the optimal reaction parameters can be challenging due to the complex interplay between reaction kinetics, mass transport, and electrochemical behavior. Furthermore, the optimal conditions for one catalyst may not be suitable for another, emphasizing the need for tailored optimization strategies based on the specific catalyst and reaction system. Developing standardized guidelines or recommendations for reaction conditions would provide a starting point for researchers and help establish more consistent and comparable results across different studies.

5) Scaling up the fabrication of catalysts is crucial for practical applications of eNO$_3$RR. While laboratory-scale synthesis methods may be suitable for initial studies, they may not be feasible for large-scale production. Therefore, it is essential to explore and develop fabrication methods compatible with industrial processes capable of producing large quantities of catalyst materials. This includes considering factors such as cost-effectiveness, scalability, reproducibility, and stability of the catalysts. Encouraging collaborations between fundamental researchers and industry partners can also facilitate the translation of research findings into practical applications. Researchers can bridge the gap between laboratory-scale synthesis and practical large-scale production by focusing on these factors and developing fabrication methods that address them.

6) Integrating computational and combinatorial approaches allows for a more efficient and systematic catalyst design and optimization exploration. The computational approach involves utilizing computational modeling and simulations to understand the fundamental mechanisms and properties of catalyst materials at the atomic and molecular levels. This enables researchers to predict and evaluate various candidate materials' catalytic activity, selectivity, and stability. Combinatorial approaches involve synthesizing and testing large libraries of catalysts with systematically varied parameters, such as composition, dopants, and nanostructure. This parallel processing enables rapid exploration of a vast design space, accelerating the discovery of catalysts with desirable properties. This combination of computational prediction and experimental validation accelerates the discovery and optimization of multifunctional nanostructured catalysts for eNO$_3$RR.

CRediT authorship contribution statement

Dong Chen: Conceptualization, Writing – original draft, Writing – review & editing. **Di Yin:** Conceptualization, Writing – original draft, Writing – review & editing. **Shaoce Zhang:** Writing – original draft, Writing – review & editing. **SenPo Yip:** Writing – original draft, Writing – review & editing. **Johnny C. Ho:** Conceptualization, Funding acquisition, Supervision, Writing – original draft, Writing – review & editing.

Declaration of competing interest

The authors declare that they have no known competing financial interests or personal relationships that could have appeared to influence the work reported in this paper.

Data availability

This is a review paper.

Acknowledgement

References

[1] Y.-M. Wei, K. Chen, J.-N. Kang, W. Chen, X.-Y. Wang, X. Zhang, Policy and management of carbon peaking and carbon neutrality: a literature review, Engineering 14 (2022) 52–63, https://doi.org/10.1016/j.eng.2021.12.018.

[2] Q. Hassan, A.Z. Sameen, H.M. Salman, M. Jaszczur, A.K. Al-Jiboory, Hydrogen energy future: advancements in storage technologies and implications for sustainability, J. Energy Storage 72 (2023) 108404, https://doi.org/10.1016/j.est.2023.108404.

[3] P.F. Borowski, B. Karlikowska, Clean hydrogen is a challenge for enterprises in the era of low-emission and zero-emission economy, Energies 16 (2023) 1171, https://doi.org/10.3390/en16031171.

[4] M. Zoback, D. Smit, Meeting the challenges of large-scale carbon storage and hydrogen production, Proc. Nat. Acad. Sci. 120 (2023) e2202397120, https://doi.org/10.1073/pnas.220239712.

[5] M. Asif, S.S. Bibi, S. Ahmed, M. Irshad, M.S. Hussain, H. Zeb, M.K. Khan, J. Kim, Recent advances in green hydrogen production, storage and commercial-scale use via catalytic ammonia cracking, Chem. Eng. J. (2023) 145381, https://doi.org/10.1016/j.cej.2023.145381.

[6] A. Klerke, C.H. Christensen, J.K. Nørskov, T. Vegge, Ammonia for hydrogen storage: challenges and opportunities, J. Mater. Chem. 18 (2008) 2304–2310, https://doi.org/10.1039/B720020J.

[7] S.L. Foster, S.I.P. Bakovic, R.D. Duda, S. Maheshwari, R.D. Milton, S.D. Minteer, M.J. Janik, J.N. Renner, L.F. Greenlee, Catalysts for nitrogen reduction to ammonia, Nat. Catal. 1 (2018) 490–500, https://doi.org/10.1038/s41929-018-0092-7.

[8] B.H. Suryanto, H.-L. Du, D. Wang, J. Chen, A.N. Simonov, D.R. MacFarlane, Challenges and prospects in the catalysis of electroreduction of nitrogen to ammonia, Nat. Catal. 2 (2019) 290–296, https://doi.org/10.1038/s41929-019-0252-4.

[9] M. Kitano, Y. Inoue, Y. Yamazaki, F. Hayashi, S. Kanbara, S. Matsuishi, T. Yokoyama, S.-W. Kim, M. Hara, H. Hosono, Ammonia synthesis using a stable electride as an electron donor and reversible hydrogen store, Nat. Chem. 4 (2012) 934–940, https://doi.org/10.1038/nchem.1476.

[10] G. Soloveichik, Electrochemical synthesis of ammonia as a potential alternative to the Haber–Bosch process, Nat. Catal. 2 (2019) 377–380, https://doi.org/10.1038/s41929-019-0280-0.

[11] X. Liu, A. Elgowainy, M. Wang, Life cycle energy use and greenhouse gas emissions of ammonia production from renewable resources and industrial by-products, Green Chem. 22 (2020) 5751–5761, https://doi.org/10.1039/D0GC02301A.

[12] S. Chatterjee, R.K. Parsapur, K.-W. Huang, Limitations of ammonia as a hydrogen energy carrier for the transportation sector, ACS Energy Lett. 6 (2021) 4390–4394, https://doi.org/10.1021/acsenergylett.1c02189.

[13] D. Bao, Q. Zhang, F.L. Meng, H.X. Zhong, M.M. Shi, Y. Zhang, J.M. Yan, Q. Jiang, X.B. Zhang, Electrochemical reduction of N$_2$ under ambient conditions for artificial N$_2$ fixation and renewable energy storage using N$_2$/NH$_3$ cycle, Adv. Mater. 29 (2017) 1604799, https://doi.org/10.1002/adma.201604799.

[14] H.K. Lee, C.S.L. Koh, Y.H. Lee, C. Liu, I.Y. Phang, X. Han, C.-K. Tsung, X.Y. Ling, Favoring the unfavored: selective electrochemical nitrogen fixation using a reticular chemistry approach, Sci. Adv. 4 (2018) eaar3208, https://doi.org/10.1126/sciadv.aar3208.

[15] X. Zhao, G. Hu, G.F. Chen, H. Zhang, S. Zhang, H. Wang, Comprehensive understanding of the thriving ambient electrochemical nitrogen reduction reaction, Adv. Mater. 33 (2021) 2007650, https://doi.org/10.1002/adma.202007650.

[16] P.H. van Langevelde, I. Katsounaros, M.T. Koper, Electrocatalytic nitrate reduction for sustainable ammonia production, Joule 5 (2021) 290–294, https://doi.org/10.1016/j.joule.2020.12.025.

[17] Y. Wang, C. Wang, M. Li, Y. Yu, B. Zhang, Nitrate electroreduction: mechanism insight, in situ characterization, performance evaluation, and challenges, Chem. Soc. Rev. 50 (2021) 6720–6733, https://doi.org/10.1039/D1CS00116G.

[18] C. Lv, J. Liu, C. Lee, Q. Zhu, J. Xu, H. Pan, C. Xue, Q. Yan, Emerging p-block-element-based electrocatalysts for sustainable nitrogen conversion, ACS Nano. 16 (2022) 15512–15527, https://doi.org/10.1021/acsnano.2c07260.

[19] D. De, E.E. Kalu, P.P. Tarjan, J.D. Englehardt, Kinetic studies of the electrochemical treatment of nitrate and nitrite ions on iridium-modified carbon fiber electrodes, Chem. Eng. Technol. Ind. Chem. Plant Equip. Process Eng. Biotechnol. 27 (2004) 56–64, https://doi.org/10.1002/ceat.200401832.

[20] M. Da Cunha, M. Weber, F.C. Nart, On the adsorption and reduction of NO3− ions at Au and Pt electrodes studied by in situ FTIR spectroscopy, J. Electroanal. Chem. 414 (1996) 163–170, https://doi.org/10.1016/0022-0728(96)04697-9.

[21] H. Huang, M. Zhao, X. Xing, I. Bae, D. Scherson, In situ infrared studies of the Cd-UPD mediated reduction of nitrate on gold, J. Electroanal. Chem. Interfacial Electrochem. 293 (1990) 279–284, https://doi.org/10.1016/0022-0728(90)80071-D.

[22] M. Duca, M.T. Koper, Powering denitrification: the perspectives of electrocatalytic nitrate reduction, Energy Environ. Sci. 5 (2012) 9726–9742, https://doi.org/10.1039/C2EE23062C.

[23] V. Rosca, M. Duca, M.T. de Groot, M.T. Koper, Nitrogen cycle electrocatalysis, Chem. Rev. 109 (2009) 2209–2244, https://doi.org/10.1021/cr8003696.

[24] M. De Groot, M. Koper, The influence of nitrate concentration and acidity on the electrocatalytic reduction of nitrate on platinum, J. Electroanal. Chem. 562 (2004) 81–94, https://doi.org/10.1016/j.jelechem.2003.08.011.

[25] J.-X. Liu, D. Richards, N. Singh, B.R. Goldsmith, Activity and selectivity trends in electrocatalytic nitrate reduction on transition metals, ACS Catal. 9 (2019) 7052–7064, https://doi.org/10.1021/acscatal.9b02179.

[26] Q. Wang, K. Yue, X. Zhang, L. Wang, M.D. Guiver, J. Zhang, Carbon fiber paper supported nano-Pt electrode with high electrocatalytic activity for concentrated nitric acid reduction, J. Electroanal. Chem. 794 (2017) 43–48, https://doi.org/10.1016/j.jelechem.2017.03.043.

[27] S. Mishra, F. Lawrence, C. Mallika, N. Pandey, R. Srinivasan, U.K. Mudali, R. Natarajan, Kinetics of reduction of nitric acid by electrochemical method and validation of cell design for plant application, Electrochim. Acta 160 (2015) 219–226, https://doi.org/10.3390/s17081908.

[28] S.-E. Bae, K.L. Stewart, A.A. Gewirth, Nitrate adsorption and reduction on Cu (100) in acidic solution, J. Am. Chem. Soc. 129 (2007) 10171–10180, https://doi.org/10.1021/ja071330n.

[29] K. Ota, Y. Amano, M. Aikawa, M. Machida, Removal of nitrate ions from water by activated carbons (ACs)-Influence of surface chemistry of ACs and coexisting chloride and sulfate ions, Appl. Surf. Sci. 276 (2013) 838–842, https://doi.org/10.1016/j.apsusc.2013.03.053.

[30] A. Waheed, N. Baig, N. Ullah, W. Falath, Removal of hazardous dyes, toxic metal ions and organic pollutants from wastewater by using porous hyper-cross-linked polymeric materials: a review of recent advances, J. Environ. Manag. 287 (2021) 112360, https://doi.org/10.1016/j.jenvman.2021.112360.

[31] J. Gao, B. Jiang, C. Ni, Y. Qi, X. Bi, Enhanced reduction of nitrate by noble metal-free electrocatalysis on P doped three-dimensional Co3O4 cathode: mechanism exploration from both experimental and DFT studies, Chem. Eng. J. 382 (2020) 123034, https://doi.org/10.1016/j.cej.2019.123034.

[32] D. Richards, S.D. Young, B.R. Goldsmith, N. Singh, Electrocatalytic nitrate reduction on rhodium sulfide compared to Pt and Rh in the presence of chloride, Catal. Sci. Technol. 11 (2021) 7331–7346, https://doi.org/10.1039/D1CY01369F.

[33] W. Zheng, L. Zhu, Z. Yan, Z. Lin, Z. Lei, Y. Zhang, H. Xu, Z. Dang, C. Wei, C. Feng, Self-activated Ni cathode for electrocatalytic nitrate reduction to ammonia: from fundamentals to scale-up for treatment of industrial wastewater, Environ. Sci. Technol. 55 (2021) 13231–13243, https://doi.org/10.1021/acs.est.1c02278.

[34] A. De Vooys, R. Van Santen, J. Van Veen, Electrocatalytic reduction of NO3 on palladium/copper electrodes, J. Mol. Catal. Chem. 154 (2000) 203–215, https://doi.org/10.1016/S1381-1169(99)00375-1.

[35] J. Liu, Z. Li, C. Lv, X.-Y. Tan, C. Lee, X.J. Loh, M.H. Chua, Z. Li, H. Pan, J. Chen, Electrocatalytic upgrading of nitrogenous wastes into value-added chemicals: a review, Mater. Today 73 (2024) 208–259, https://doi.org/10.1016/j.mattod.2024.01.009.

[36] W. Yu, J. Yu, M. Huang, Y. Wang, Y. Wang, J. Li, H. Liu, W. Zhou, Laser-controlled tandem catalytic sites of CuNi alloys with ampere-level electrocatalytic nitrate-to-ammonia reduction activities for Zn–nitrate batteries, Energy Environ. Sci. 16 (2023) 2991–3001, https://doi.org/10.1039/D3EE01301D.

[37] X. Li, H.Y. Wang, H. Yang, W. Cai, S. Liu, B. Liu, *In situ*/operando characterization techniques to probe the electrochemical reactions for energy conversion, Small Methods. 2 (2018) 1700395, https://doi.org/10.1002/smtd.201700395.

[38] R. Yuan, H. Jiao, H. Zhu, D. Fang, S. Jiao, *In situ* characterization techniques and methodologies for high-temperature electrochemistry, Chem 9 (2023) 2481–2508, https://doi.org/10.1016/j.chempr.2023.06.018.

[39] X. Ma, W. Luo, M. Yan, L. He, L. Mai, *In situ* characterization of electrochemical processes in one dimensional nanomaterials for energy storages devices, Nano Energy. 24 (2016) 165–188, https://doi.org/10.1016/j.nanoen.2016.03.023.

[40] S. Möller, S. Barwe, J. Masa, D. Wintrich, S. Seisel, H. Baltruschat, W. Schuhmann, Online monitoring of electrochemical carbon corrosion in alkaline electrolytes by differential electrochemical mass spectrometry, Angew. Chem. Int. Ed. 59 (2020) 1585–1589, https://doi.org/10.1002/anie.201909475.

[41] E. Castaneda-Morales, J.O. Peralta-Cruz, F. Ruiz-Zepeda, A. Susarrey-Arce, M.L. Hernández-Pichardo, A. Manzo-Robledo, Electrochemical reduction of NO3 to NH3 using defect-rich TiO2 support loaded with CuNi catalysts: differential electrochemical mass spectrometry insights, Mater. Today Energy 41 (2024) 101525, https://doi.org/10.1016/j.mtener.2024.101525.

[42] T. Li, S. Han, Y. Wang, J. Zhou, B. Zhang, Y. Yu, A spectroscopic study on nitrogen electrooxidation to nitrate, Angew. Chem. Int. Ed. 62 (2023) e202217411, https://doi.org/10.1002/anie.202217411.

[43] S. Kim, H.S. Kim, B. Kim, Y.J. Kim, J.W. Jung, W.H. Ryu, *In situ* gas analysis by differential electrochemical mass spectrometry for advanced rechargeable batteries: a review, Adv. Energy Mater. 13 (2023) 2301983, https://doi.org/10.1002/aenm.202370157.

[44] L. Liu, S.J. Zheng, H. Chen, J. Cai, S.Q. Zang, Tandem nitrate-to-ammonia conversion on atomically precise silver nanocluster/MXene electrocatalyst, Angew. Chem. Int. Ed. 63 (2024) e202316910, https://doi.org/10.1002/anie.202316910.

[45] K. Fan, W. Xie, J. Li, Y. Sun, P. Xu, Y. Tang, Z. Li, M. Shao, Active hydrogen boosts electrochemical nitrate reduction to ammonia, Nat. Commun. 13 (2022) 7958, https://doi.org/10.1038/s41467-022-35664-w.

[46] X. Zhang, C. Wang, Y. Guo, B. Zhang, Y. Wang, Y. Yu, Cu clusters/TiO2-x with abundant oxygen vacancies for enhanced electrocatalytic nitrate reduction to ammonia, J. Mater. Chem. 10 (2022) 6448–6453, https://doi.org/10.1039/D2TA00661H.

[47] H. Liu, X. Lang, C. Zhu, J. Timoshenko, M. Rüscher, L. Bai, N. Guijarro, H. Yin, Y. Peng, J. Li, Efficient electrochemical nitrate reduction to ammonia with copper supported rhodium cluster and single-atom catalysts, Angew. Chem. 23 (2022) e202202556, https://doi.org/10.1002/anie.202202556.

[48] J.-T. Li, Z.-Y. Zhou, I. Broadwell, S.-G. Sun, *In situ* infrared spectroscopic studies of electrochemical energy conversion and storage, Acc. Chem. Res. 45 (2012) 485–494, https://doi.org/10.1021/ar200215t.

[49] M.A. Mohamed, J. Jaafar, A. Ismail, M. Othman, M. Rahman, Fourier Transform Infrared (FTIR) Spectroscopy, Membrane Characterization, Elsevier, 2017, pp. 3–29.

[50] T. Iwasita, F.C. Nart, In-situ fourier transform infrared spectroscopy: a tool to characterize the metal-electrolyte interface at a molecular level, Adv. Electrochem. Sci. Eng. 4 (1995) 123–216.

[51] Y. Zhang, Y. Katayama, R. Tatara, L. Giordano, Y. Yu, D. Fraggedakis, J.G. Sun, F. Maglia, R. Jung, M.Z. Bazant, Revealing electrolyte oxidation via carbonate dehydrogenation on Ni-based oxides in Li-ion batteries by in situ Fourier transform infrared spectroscopy, Energy Environ. Sci. 13 (2020) 183–199, https://doi.org/10.1039/C9EE02543J.

[52] K. Adarsh, N. Chandrasekaran, V. Chakrapani, *In situ* spectroscopic techniques as critical evaluation tools for electrochemical carbon dioxide reduction: a mini review, Front. Chem. 8 (2020) 137, https://doi.org/10.3389/fchem.2020.00137.

[53] Y. Zhang, H. Zheng, K. Zhou, J. Ye, K. Chu, Z. Zhou, L. Zhang, T. Liu, Conjugated coordination polymer as a new platform for efficient and selective electroreduction of nitrate into ammonia, Adv. Mater. 35 (2023) 2209855, https://doi.org/10.1002/adma.202209855.

[54] Q. Hu, K. Yang, O. Peng, M. Li, L. Ma, S. Huang, Y. Du, Z.-X. Xu, Q. Wang, Z. Chen, M. Yang, K.P. Loh, Ammonia electrosynthesis from nitrate using a ruthenium-copper cocatalyst system: a full concentration range study, J. Am. Chem. Soc. 146 (2023) 668–676, https://doi.org/10.1021/jacs.3c10516.

[55] W. Pech-Rodríguez, D. González-Quijano, G. Vargas-Gutiérrez, C. Morais, T. Napporn, F. Rodríguez-Varela, Electrochemical and in situ FTIR study of the ethanol oxidation reaction on PtMo/C nanomaterials in alkaline media, Appl. Catal., B 203 (2017) 654–662, https://doi.org/10.1016/j.apcatb.2016.10.058.

[56] Z.-Y. Zhou, Q. Wang, J.-L. Lin, N. Tian, S.-G. Sun, *In situ* FTIR spectroscopic studies of electrooxidation of ethanol on Pd electrode in alkaline media, Electrochim. Acta 55 (2010) 7995–7999, https://doi.org/10.1016/j.electacta.2010.02.071.

[57] G. Zhang, X. Li, K. Chen, Y. Guo, D. Ma, K. Chu, Tandem electrocatalytic nitrate reduction to ammonia on MBenes, Angew. Chem. Int. Ed. 62 (2023) e202300054, https://doi.org/10.1002/anie.202300054.

[58] J.-Y. Fang, Q.-Z. Zheng, Y.-Y. Lou, K.-M. Zhao, S.-N. Hu, G. Li, O. Akdim, X.-Y. Huang, S.-G. Sun, Ampere-level current density ammonia electrochemical synthesis using CuCo nanosheets simulating nitrite reductase bifunctional nature, Nat. Commun. 13 (2022) 7899, https://doi.org/10.1038/s41467-022-35533-6.

[59] M.C. Figueiredo, J. Souza-Garcia, V. Climent, J.M. Feliu, Nitrate reduction on Pt (1 1 1) surfaces modified by Bi adatoms, Electrochem. Commun. 11 (2009) 1760–1763, https://doi.org/10.1016/j.elecom.2009.07.010.

[60] E. Pérez-Gallent, M.C. Figueiredo, I. Katsounaros, M.T. Koper, Electrocatalytic reduction of Nitrate on Copper single crystals in acidic and alkaline solutions, Electrochim. Acta 227 (2017) 77–84, https://doi.org/10.1016/j.electacta.2016.12.147.

[61] V. Rosca, G.L. Beltramo, M.T. Koper, Hydroxylamine electrochemistry at polycrystalline platinum in acidic media: a voltammetric, DEMS and FTIR study, J. Electroanal. Chem. 566 (2004) 53–62, https://doi.org/10.1016/j.jelechem.2003.11.011.

[62] L. Yang, L. Hu, Y. Nie, J. Qu, Surface acidity and reactivity of β-FeOOH/Al2O3 for pharmaceuticals degradation with ozone: i*In situ* ATR-FTIR studies, Appl. Catal. B 97 (2010) 340–346, https://doi.org/10.1016/j.apcatb.2010.04.014.

[63] Z.-Y. Zhou, N. Tian, Y.-J. Chen, S.-P. Chen, S.-G. Sun, *In situ* rapid-scan time-resolved microscope FTIR spectroelectrochemistry: study of the dynamic processes of methanol oxidation on a nanostructured Pt electrode, J. Electroanal. Chem. 573 (2004) 111–119, https://doi.org/10.1016/j.jelechem.2004.07.003.

[64] Y. Yao, S. Zhu, H. Wang, H. Li, M. Shao, A spectroscopic study on the nitrogen electrochemical reduction reaction on gold and platinum surfaces, J. Am. Chem. Soc. 140 (2018) 1496–1501, https://doi.org/10.1021/jacs.7b12101.

[65] S. Zhu, X. Qin, F. Xiao, S. Yang, Y. Xu, Z. Tan, J. Li, J. Yan, Q. Chen, M. Chen, The role of ruthenium in improving the kinetics of hydrogen oxidation and evolution reactions of platinum, Nat. Catal. 4 (2021) 711–718, https://doi.org/10.1038/s41929-021-00663-5.

[66] M. Chiesa, E. Giamello, M. Che, EPR characterization and reactivity of surface-localized inorganic radicals and radical ions, Chem. Rev. 110 (2010) 1320–1347, https://doi.org/10.1021/cr800366v.

[67] R. Konaka, M. Kawai, H. Noda, M. Kohno, R. Niwa, Synthesis and evaluation of DMPO-type spin traps, Free Radic. Res. 23 (1995) 15–25, https://doi.org/10.3109/10715769509064015.

[68] N. Zhang, G. Zhang, P. Shen, H. Zhang, D. Ma, K. Chu, Lewis acid Fe-V pairs promote nitrate electroreduction to ammonia, Adv. Funct. Mater. 33 (2023) 2211537, https://doi.org/10.1002/adfm.202211537.

[69] Z. Gu, Y. Zhang, X. Wei, Z. Duan, Q. Gong, K. Luo, Intermediates regulation via electron-deficient Cu sites for selective nitrate-to-ammonia electro-reduction, Adv. Mater. 35 (2023) 2303107, https://doi.org/10.1002/adma.202303107.

[70] X. Li, P. Shen, X. Li, D. Ma, K. Chu, Sub-nm RuOx clusters on Pd metallene for synergistically enhanced nitrate electroreduction to ammonia, ACS Nano. 17 (2023) 1081–1090, https://doi.org/10.1021/acsnano.2c07911.

[71] Y. Wang, D. Zhao, H. Ji, G. Liu, C. Chen, W. Ma, H. Zhu, J. Zhao, Sonochemical hydrogen production efficiently catalyzed by Au/TiO₂, J. Phys. Chem. C 114 (2010) 17728–17733, https://doi.org/10.1021/jp105691v.

[72] M. Kohno, T. Mokudai, T. Ozawa, Y. Niwano, Free radical formation from sonolysis of water in the presence of different gases, J. Clin. Biochem. Nutr. 49 (2011) 96–101, https://doi.org/10.3164/jcbn.10-130.

[73] S. Zhang, D. Chen, Y. Guo, R. Zhang, Y. Zhao, Z. Huang, J. Fan, J.C. Ho, C. Zhi, Piezoelectricity regulated ohmic contact in M/BaTiO₃ (M= Ru, Pd, Pt) for charge collision and hydrogen free radical production in ammonia electro-synthesis, Mater. Today 66 (2023) 17–25, https://doi.org/10.1016/j.mattod.2023.03.011.

[74] M.J. Davies, Detection and characterisation of radicals using electron para-magnetic resonance (EPR) spin trapping and related methods, Methods 109 (2016) 21–30, https://doi.org/10.1016/j.ymeth.2016.05.013.

[75] I.E. Wachs, In situ Raman spectroscopy studies of catalysts, Top. Catal. 8 (1999) 57–63, https://doi.org/10.1023/A:1019100925300.

[76] J. Wu, L. Xu, Z. Kong, K. Gu, Y. Lu, X. Wu, Y. Zou, S. Wang, Integrated tandem electrochemical-chemical-electrochemical coupling of biomass and nitrate to sustainable alanine, Angew. Chem. 135 (2023) e202311196, https://doi.org/10.1002/ange.202311196.

[77] H. Knözinger, G. Mestl, Laser Raman spectroscopy—a powerful tool for in situ studies of catalytic materials, Top. Catal. 8 (1999) 45–55, https://doi.org/10.1023/A:1019184321666.

[78] X.D. Lin, V. Uzayisenga, J.F. Li, P.P. Fang, D.Y. Wu, B. Ren, Z.Q. Tian, Synthesis of ultrathin and compact Au@ MnO₂ nanoparticles for shell-isolated nano-particle-enhanced Raman spectroscopy (SHINERS), J. Raman Spectrosc. 43 (2012) 40–45, https://doi.org/10.1002/jrs.3007.

[79] Y. Kim, J. Ko, M. Shim, J. Park, H.-H. Shin, Z.H. Kim, Y. Jung, H.R. Byon, Identifying the active sites and intermediates on copper surfaces for elec-trochemical nitrate reduction to ammonia, Chem. Sci. 15 (2024) 2578–2585, https://doi.org/10.1039/D3SC05793C.

[80] Y. Zhao, X. Chang, A.S. Malkani, X. Yang, L. Thompson, F. Jiao, B. Xu, Speciation of Cu surfaces during the electrochemical CO reduction reac-tion, J. Am. Chem. Soc. 142 (2020) 9735–9743, https://doi.org/10.1021/jacs.0c02354.

[81] N. Wen, M.H. Brooker, Ammonium carbonate, ammonium bicarbonate, and ammonium carbamate equilibria: a Raman study, J. Phys. Chem. 99 (1995) 359–368, https://doi.org/10.1021/j100001a054.

[82] D. Chen, S. Zhang, D. Yin, W. Li, X. Bu, Q. Quan, Z. Lai, W. Wang, Y. Meng, C. Liu, Tailored p-orbital delocalization by diatomic Pt-Ce induced interlayer spacing engineering for highly-efficient ammonia electrosynthesis, Adv. Energy Mater. 13 (2023) 2203201, https://doi.org/10.1002/aenm.202203201.

[83] Y. Zheng, T. Deng, N. Yue, W. Zhang, X. Zhu, H. Huang, X. Chu, W. Zheng, Raman spectroscopy and correlative-Raman technology excel as an optimal stage for carbon-based electrode materials in electrochemical energy stor-age, J. Raman Spectrosc. 52 (2021) 2119–2130, https://doi.org/10.1002/jrs.6178.

[84] D. Philip, A. Eapen, G. Aruldhas, Vibrational and surface enhanced Raman scattering spectra of sulfamic acid, J. Solid State Chem. 116 (1995) 217–223, https://doi.org/10.1006/jssc.1995.1206.

[85] W. Gao, K. Xie, J. Xie, X. Wang, H. Zhang, S. Chen, H. Wang, Z. Li, C. Li, Alloying of Cu with Ru enabling the relay catalysis for reduction of nitrate to ammonia, Adv. Mater. 35 (2023) 2202952, https://doi.org/10.1002/adma.202202952.

[86] D.P. Butcher Jr., A.A. Gewirth, Nitrate reduction pathways on Cu single crystal surfaces: effect of oxide and Cl⁻, Nano Energy. 29 (2016) 457–465, https://doi.org/10.1016/j.nanoen.2016.06.024.

[87] T.J. Dines, C.H. Rochester, A.M. Ward, Infrared and Raman study of the adsorption of NH₃, pyridine, NO and NO₂ on anatase, J. Chem. Soc., Faraday Trans. 87 (1991) 643–651, https://doi.org/10.1039/FT9918700643.

[88] N. Sergent, M. Epifani, T. Pagnier, In situ Raman spectroscopy study of NO₂ adsorption onto nanocrystalline tin (IV) oxide, J. Raman Spectrosc. 37 (2006) 1272–1277, https://doi.org/10.1002/jrs.1548.

[89] G. Fevotte, In situ Raman spectroscopy for in-line control of pharmaceutical crystallization and solids elaboration processes: a review, Chem. Eng. Res. Des. 85 (2007) 906–920, https://doi.org/10.1205/cherd06229.

[90] H.-T. Lien, S.-T. Chang, P.-T. Chen, D.P. Wong, Y.-C. Chang, Y.-R. Lu, C.-L. Dong, C.-H. Wang, K.-H. Chen, L.-C. Chen, Probing the active site in single-atom oxygen reduction catalysts via operando X-ray and electrochemical spec-troscopy, Nat. Commun. 11 (2020) 4233, https://doi.org/10.1038/s41467-020-17975-y.

[91] L. Fang, S. Seifert, R.E. Winans, T. Li, Understanding synthesis and structural variation of nanomaterials through in situ/operando XAS and SAXS, Small 18 (2022) 2106017, https://doi.org/10.1002/smll.202106017.

[92] Y. Zhu, T.-R. Kuo, Y.-H. Li, M.-Y. Qi, G. Chen, J. Wang, Y.-J. Xu, H.M. Chen, Emerging dynamic structure of electrocatalysts unveiled by in situ X-ray diffraction/absorption spectroscopy, Energy Environ. Sci. 14 (2021) 1928–1958, https://doi.org/10.1039/D0EE03903A.

[93] J. Yang, H. Qi, A. Li, X. Liu, X. Yang, S. Zhang, Q. Zhao, Q. Jiang, Y. Su, L. Zhang, Potential-driven restructuring of Cu single atoms to nanoparticles for boosting the electrochemical reduction of nitrate to ammonia, J. Am. Chem. Soc. 144 (2022) 12062–12071, https://doi.org/10.1021/jacs.2c02262.

[94] J. Yang, W. Liu, M. Xu, X. Liu, H. Qi, L. Zhang, X. Yang, S. Niu, D. Zhou, Y. Liu, Dynamic behavior of single-atom catalysts in electrocatalysis: identification of Cu-N₃ as an active site for the oxygen reduction reaction, J. Am. Chem. Soc. 143 (2021) 14530–14539, https://doi.org/10.1021/jacs.1c03788.

[95] W.-Y. Ko, W.-H. Chen, C.-Y. Cheng, K.-J. Lin, Architectural growth of Cu nanoparticles through electrodeposition, Nanoscale Res. Lett. 4 (2009) 1481–1485, https://doi.org/10.1007/s11671-009-9424-5.

[96] Y. Lum, J.W. Ager, Stability of residual oxides in oxide-derived copper cata-lysts for electrochemical CO₂ reduction investigated with ¹⁸O labeling, Angew. Chem. Int. Ed. 57 (2018) 551–554, https://doi.org/10.1002/anie.201710590.

[97] T. Zhu, Q. Chen, P. Liao, W. Duan, S. Liang, Z. Yan, C. Feng, Single-atom Cu catalysts for enhanced electrocatalytic nitrate reduction with significant alleviation of nitrite production, Small 16 (2020) 2004526, https://doi.org/10.1002/smll.202004526.

[98] G.-F. Chen, Y. Yuan, H. Jiang, S.-Y. Ren, L.-X. Ding, L. Ma, T. Wu, J. Lu, H. Wang, Electrochemical reduction of nitrate to ammonia via direct eight-electron transfer using a copper–molecular solid catalyst, Nat. Energy 5 (2020) 605–613, https://doi.org/10.1038/s41560-020-0654-1.

[99] J. Shao, H. Jing, P. Wei, X. Fu, L. Pang, Y. Song, K. Ye, M. Li, L. Jiang, J. Ma, R. Li, R. Si, Z. Peng, G. Wang, J. Xiao, Electrochemical synthesis of ammonia from nitric oxide using a copper-tin alloy catalyst, Nat. Energy 8 (2023) 1273–1283, https://doi.org/10.1038/s41560-023-01386-6.

[100] B. Yang, W. Ding, H. Zhang, S. Zhang, Recent progress in electrochemical synthesis of ammonia from nitrogen: strategies to improve the catalytic activity and selectivity, Energy Environ. Sci. 14 (2021) 672–687, https://doi.org/10.1039/D0EE02263B.

[101] D. Zhao, J. Yao, C. Ma, A. Wang, H. Xie, J. Zhao, J. Yan, K. Zhu, Y. Zhu, D. Cao, 3D integrated non-noble metal oxides nano arrays for enhanced nitrate elec-troreduction to ammonia, J. Power Sources 592 (2024) 233945, https://doi.org/10.1016/j.jpowsour.2023.233945.

[102] Y. Gao, Z. Xiao, D. Kong, R. Iqbal, Q.-H. Yang, L. Zhi, N, P co-doped hollow carbon nanofiber membranes with superior mass transfer property for tri-functional metal-free electrocatalysis, Nano Energy. 64 (2019) 103879, https://doi.org/10.1016/j.nanoen.2019.103879.

[103] J. Le Xie, C.X. Guo, C.M. Li, Construction of one-dimensional nanostructures on graphene for efficient energy conversion and storage, Energy Environ. Sci. 7 (2014) 2559–2579, https://doi.org/10.1039/C4EE00531G.

[104] H. Wu, C. Feng, L. Zhang, J. Zhang, D.P. Wilkinson, Non-noble metal elec-trocatalysts for the hydrogen evolution reaction in water electrolysis, Elec-tro, Energy Rev. 4 (2021) 473–507, https://doi.org/10.1007/s41918-020-00086-z.

[105] H. Zhang, C. Wang, H. Luo, J. Chen, M. Kuang, J. Yang, Iron nanoparticles protected by chainmail-structured graphene for durable electrocatalytic ni-trate reduction to nitrogen, Angew. Chem. 135 (2023) e202217071, https://doi.org/10.1002/anie.202217071.

[106] X. Liu, Y. Wang, R.L. Smith Jr., L. Liu, X. Qi, Synthesis of self-renewing Fe (0)-dispersed ordered mesoporous carbon for electrocatalytic reduction of ni-trates to nitrogen, Sci. Total Environ. 836 (2022) 155640, https://doi.org/10.1016/j.scitotenv.2022.155640.

[107] J. Lu, X. Liu, H. Zhang, M. Fu, H. Zheng, Q. Chen, J. Zhou, Electrocatalytic ac-tivity of nano-flowered yavapaiite anchored on magnetic graphite oxide for nitrate selective reduction, Chem. Eng. J. 433 (2022) 134586, https://doi.org/10.1016/j.cej.2022.134586.

[108] R. Zhao, Q. Yan, L. Yu, T. Yan, X. Zhu, Z. Zhao, L. Liu, J. Xi, A Bi-Co corridor construction effectively improving the selectivity of electrocatalytic nitrate reduction toward ammonia by nearly 100%, Adv. Mater. 35 (2023) 2306633 https://doi.org/10.1002/adma.202306633.

[109] Y. Yoon, A.S. Hall, Y. Surendranath, Tuning of silver catalyst mesostructure promotes selective carbon dioxide conversion into fuels, Angew. Chem. Int. Ed. 55 (2016) 15282–15286, https://doi.org/10.1002/anie.201607942.

[110] F. Naseem, P. Lu, J. Zeng, Z. Lu, Y.H. Ng, H. Zhao, Y. Du, Z. Yin, Solid nano-porosity governs catalytic CO₂ and N₂ reduction, ACS Nano. 14 (2020) 7734–7759, https://doi.org/10.1021/acsnano.0c02731.

[111] J. Wordsworth, T.M. Benedetti, S.V. Somerville, W. Schuhmann, R.D. Tilley, J.J. Gooding, The influence of nanoconfinement on electrocatalysis, Angew. Chem. Int. Ed. 61 (2022) e202200755, https://doi.org/10.1002/anie.202200755.

[112] P.B. O'Mara, P. Wilde, T.M. Benedetti, C. Andronescu, S. Cheong, J.J. Gooding, R.D. Tilley, W. Schuhmann, Cascade reactions in nanozymes: spatially separated active sites inside Ag-Core-Porous-Cu-shell nanoparticles for multistep carbon dioxide reduction to higher organic molecules, J. Am. Chem. Soc. 141 (2019) 14093–14097, https://doi.org/10.1021/jacs.9b07310.

[113] L. Sun, B. Liu, Mesoporous PdN alloy nanocubes for efficient electrochemical nitrate reduction to ammonia, Adv. Mater. 35 (2023) 2207305, https://doi.org/10.1002/adma.202207305.

[114] S. De, S. Acharya, S. Sahoo, J.-J. Shim, G.C. Nayak, From 0D to 3D MXenes: their diverse syntheses, morphologies and applications, Mater. Chem. Front. 6 (2022) 818–842, https://doi.org/10.1039/D2QM00002D.

[115] Y. Chen, Z. Lai, X. Zhang, Z. Fan, Q. He, C. Tan, H. Zhang, Phase engineering of nanomaterials, Nat. Rev. Chem 4 (2020) 243–256, https://doi.org/10.1038/s41570-020-0173-4.

[116] D. Chen, S. Zhang, X. Bu, R. Zhang, Q. Quan, Z. Lai, W. Wang, Y. Meng, D. Yin, S. Yip, Synergistic modulation of local environment for electrochemical nitrate reduction via asymmetric vacancies and adjacent ion clusters, Nano Energy. 98 (2022) 107338, https://doi.org/10.1016/j.nanoen.2022.107338.

[117] J. Romo-Herrera, M. Terrones, H. Terrones, S. Dag, V. Meunier, Covalent 2D and 3D networks from 1D nanostructures: designing new materials, Nano Lett. 7 (2007) 570–576, https://doi.org/10.1021/nl0622202.

[118] Q. Gao, B. Yao, H.S. Pillai, W. Zang, X. Han, Y. Liu, S.-W. Yu, Z. Yan, B. Min, S. Zhang, H. Zhou, L. Ma, H. Xin, Q. He, H. Zhu, Synthesis of core/shell nanocrystals with ordered intermetallic single-atom alloy layers for nitrate electroreduction to ammonia, Nat. Synthesis 2 (2023) 1–11, https://doi.org/10.1038/s44160-023-00258-x.

[119] W.-D. Zhang, H. Dong, L. Zhou, H. Xu, H.-R. Wang, X. Yan, Y. Jiang, J. Zhang, Z.-G. Gu, Fe single-atom catalysts with pre-organized coordination structure for efficient electrochemical nitrate reduction to ammonia, Appl. Catal., B 317 (2022) 121750, https://doi.org/10.1016/j.apcatb.2022.121750.

[120] K.M. Lodaya, B.Y. Tang, R.P. Bisbey, S. Weng, K.S. Westendorff, W.L. Toh, J. Ryu, Y. Román-Leshkov, S. Surendranath, An electrochemical approach for designing thermochemical bimetallic nitrate hydrogenation catalysts, Nat. Catal. 7 (2024) 1–11, https://doi.org/10.1038/s41929-023-01094-0.

[121] B. Pourbahari, M. Emamy, H. Mirzadeh, Synergistic effect of Al and Gd on enhancement of mechanical properties of magnesium alloys, Prog. Nat. Sci-Mater. 27 (2017) 228–235, https://doi.org/10.1016/j.pnsc.2017.02.004.

[122] Y. Wang, W. Zhou, R. Jia, Y. Yu, B. Zhang, Unveiling the activity origin of a copper-based electrocatalyst for selective nitrate reduction to ammonia, Angew. Chem. Int. Ed. 59 (2020) 5350–5354, https://doi.org/10.1002/anie.201915992.

[123] D. Zhang, B. Wang, X. Gong, Z. Yang, Y. Liu, Selective reduction of nitrate to nitrogen gas by novel $Cu_2O-Cu_0@Fe_0$ composite combined with HCOOH under UV radiation, Chem. Eng. J. 359 (2019) 1195–1204, https://doi.org/10.1016/j.cej.2018.11.058.

[124] X. Zhao, K. Zhao, X. Quan, S. Chen, H. Yu, Z. Zhang, J. Niu, S. Zhang, Efficient electrochemical nitrate removal on Cu and nitrogen doped carbon, Chem. Eng. J. 415 (2021) 128958, https://doi.org/10.1016/j.cej.2021.128958.

[125] X. Wang, M. Zhu, G. Zeng, X. Liu, C. Fang, C. Li, A three-dimensional Cu nanobelt cathode for highly efficient electrocatalytic nitrate reduction, Nanoscale 12 (2020) 9385–9391, https://doi.org/10.1039/C9NR10743F.

[126] Q. Hu, Y. Qin, X. Wang, Z. Wang, X. Huang, H. Zheng, K. Gao, H. Yang, P. Zhang, M. Shao, Reaction intermediate-mediated electrocatalyst synthesis favors specified facet and defect exposure for efficient nitrate–ammonia conversion, Energy Environ. Sci. 14 (2021) 4989–4997, https://doi.org/10.1039/D1EE01731D.

[127] K. Liu, C. Zhang, Y. Sun, G. Zhang, X. Shen, F. Zou, H. Zhang, Z. Wu, E.C. Wegener, C.J. Taubert, High-performance transition metal phosphide alloy catalyst for oxygen evolution reaction, ACS Nano. 12 (2018) 158–167, https://doi.org/10.1021/acsnano.7b04646.

[128] M.M. Kuypers, H.K. Marchant, B. Kartal, The microbial nitrogen-cycling network, Nat. Rev. Microbiol. 16 (2018) 263–276, https://doi.org/10.1038/nrmicro.2018.9.

[129] Y. Xu, K. Ren, T. Ren, M. Wang, M. Liu, Z. Wang, X. Li, L. Wang, H. Wang, Cooperativity of Cu and Pd active sites in CuPd aerogels enhances nitrate electroreduction to ammonia, Chem. Commun. 57 (2021) 7525–7528, https://doi.org/10.1039/D1CC02105B.

[130] Y. Wang, A. Xu, Z. Wang, L. Huang, J. Li, F. Li, J. Wicks, M. Luo, D.-H. Nam, C.-S. Tan, Enhanced nitrate-to-ammonia activity on copper–nickel alloys via tuning of intermediate adsorption, J. Am. Chem. Soc. 142 (2020) 5702–5708, https://doi.org/10.1021/jacs.9b13347.

[131] X. Zhao, Y. Jiang, M. Wang, S. Liu, Z. Wang, T. Qian, C. Yan, Optimizing intermediate adsorption via heteroatom ensemble effect over RuFe bimetallic alloy for enhanced nitrate electroreduction to ammonia, Adv. Energy Mater. 13 (2023) 2301409, https://doi.org/10.1002/aenm.202301409.

[132] Y. Li, C.-K. Peng, H. Hu, S.-Y. Chen, J.-H. Choi, Y.-G. Lin, J.-M. Lee, Interstitial boron-triggered electron-deficient Os aerogels for enhanced pH-universal hydrogen evolution, Nat. Commun. 13 (2022) 1143, https://doi.org/10.1038/s41467-022-28805-8.

[133] K. Chu, W. Zong, G. Xue, H. Guo, J. Qin, H. Zhu, N. Zhang, Z. Tian, H. Dong, Y.-E. Miao 12, J. Am. Chem. Soc. 145 (2023) 21387–21396, https://doi.org/10.1021/jacs.3c06402.

[134] H. Du, H. Guo, K. Wang, X. Du, B.A. Beshiwork, S. Sun, Y. Luo, Q. Liu, T. Li, X. Sun, Durable electrocatalytic reduction of nitrate to ammonia over defective pseudobrookite Fe2TiO5 nanofibers with abundant oxygen vacancies, Angew. Chem. 135 (2023) e202215782, https://doi.org/10.1002/ange.202215782.

[135] T. Wu, X. Zhu, Z. Xing, S. Mou, C. Li, Y. Qiao, Q. Liu, Y. Luo, X. Shi, Y. Zhang, Greatly improving electrochemical N_2 reduction over TiO_2 nanoparticles by iron doping, Angew. Chem. Int. Ed. 58 (2019) 18449–18453, https://doi.org/10.1002/anie.201911153.

[136] Y. Zhang, X. Chen, W. Wang, L. Yin, J.C. Crittenden, Electrocatalytic nitrate reduction to ammonia on defective Au1Cu (111) single-atom alloys, Appl. Catal. B 310 (2022) 121346, https://doi.org/10.1016/j.apcatb.2022.121346.

[137] R. Zhang, S. Zhang, Y. Guo, C. Li, J. Liu, Z. Huang, Y. Zhao, Y. Li, C. Zhi, A Zn–nitrite battery as an energy-output electrocatalytic system for high-efficiency ammonia synthesis using carbon-doped cobalt oxide nanotubes, Energy Environ. Sci. 15 (2022) 3024–3032, https://doi.org/10.1039/D2EE00686C.

[138] H. Vahidi, K. Syed, H. Guo, X. Wang, J.L. Wardini, J. Martinez, W.J. Bowman, A review of grain boundary and heterointerface characterization in polycrystalline oxides by (scanning) transmission electron microscopy, Crystals 11 (2021) 878, https://doi.org/10.3390/cryst11080878.

[139] J. Zhou, M. Wen, R. Huang, Q. Wu, Y. Luo, Y. Tian, G. Wei, Y. Fu, Regulating active hydrogen adsorbed on grain boundary defects of nano-nickel for boosting ammonia electrosynthesis from nitrate, Energy Environ. Sci. 16 (2023) 2611–2620, https://doi.org/10.1039/D2EE04095F.

[140] Y. Miao, Y. Zhao, S. Zhang, R. Shi, T. Zhang, Strain engineering: a boosting strategy for photocatalysis, Adv. Mater. 34 (2022) 2200868, https://doi.org/10.1002/adma.202200868.

[141] S. Paul, S. Sarkar, A. Adalder, S. Kapse, R. Thapa, U.K. Ghorai, Strengthening the metal center of Co-N4 active sites in a 1D-2D Heterostructure for nitrate and nitrogen reduction reaction to ammonia, ACS Sustain. Chem. Eng. 11 (2023) 6191–6200, https://doi.org/10.1021/acssuschemeng.2c07114.

[142] Q. Geng, H. Xie, Y. He, Y. Sun, X. Hou, W. Zhiming, F. Dong, Atomic interfacial structure and charge transfer mechanism on *in situ* formed $BiOI/Bi_2O_2SO_4$ p-n heterojunctions with highly promoted photocatalysis, Appl. Catal. B 297 (2021) 120492, https://doi.org/10.1016/j.apcatb.2021.120492.

[143] H. Luo, S. Li, Z. Wu, Y. Liu, W. Luo, W. Li, D. Zhang, J. Chen, J. Yang, Modulating the active hydrogen adsorption on Fe-N interface for boosted electrocatalytic nitrate reduction with ultra-long stability, Adv. Mater. 35 (2023) 2304695, https://doi.org/10.1002/adma.202304695.

[144] W.J. Sun, H.Q. Ji, L.X. Li, H.Y. Zhang, Z.K. Wang, J.H. He, J.M. Lu, Built-in electric field triggered interfacial accumulation effect for efficient nitrate removal at ultra-low concentration and electroreduction to ammonia, Angew. Chem. Int. Ed. Engl. 60 (2021) 22933–22939, https://doi.org/10.1002/anie.202109785.

[145] W. He, J. Zhang, S. Dieckhöfer, S. Varhade, A.C. Brix, A. Lielpetere, S. Seisel, J.R. Junqueira, W. Schuhmann, Splicing the active phases of copper/cobalt-based catalysts achieves high-rate tandem electroreduction of nitrate to ammonia, Nat. Commun. 13 (2022) 1–13, https://doi.org/10.1038/s41467-022-28728-4.

[146] I. Schrader, J. Warneke, J. Backenköhler, S. Kunz, Functionalization of platinum nanoparticles with L-proline: simultaneous enhancements of catalytic activity and selectivity, J. Am. Chem. Soc. 137 (2015) 905–912, https://doi.org/10.1021/ja511349p.

[147] Y.-C. Hsieh, S.D. Senanayake, Y. Zhang, W. Xu, D.E. Polyansky, Effect of chloride anions on the synthesis and enhanced catalytic activity of silver nanocoral electrodes for CO_2 electroreduction, ACS Catal. 5 (2015) 5349–5356, https://doi.org/10.1021/acscatal.5b01235.

[148] M. Zhao, H. Tang, Q. Yang, Y. Gu, H. Zhu, S. Yan, Z. Zou, Inhibiting hydrogen evolution using a chloride adlayer for efficient electrochemical CO_2 reduction on Zn electrodes, ACS Appl. Mater. Interfaces 12 (2020) 4565–4571, https://doi.org/10.1021/acsami.9b22811.

[149] A.S. Varela, W. Ju, T. Reier, P. Strasser, Tuning the catalytic activity and selectivity of Cu for CO_2 electroreduction in the presence of halides, ACS Catal. 6 (2016) 2136–2144, https://doi.org/10.1021/acscatal.5b02550.

[150] J. Wang, C. Cai, Y. Wang, X. Yang, D. Wu, Y. Zhu, M. Li, M. Gu, M. Shao, Electrocatalytic reduction of nitrate to ammonia on low-cost ultrathin CoO_x nanosheets, ACS Catal. 11 (2021) 15135–15140, https://doi.org/10.1021/acscatal.1c03918.

[151] B. Zhang, G. Zhang, B. Zhang, L. Xia, Y. Jiang, T. Ma, M. Gao, W. Sun, H. Pan, Lattice-confined Ir clusters on Pd nanosheets with charge redistribution for the hydrogen oxidation reaction under alkaline conditions, Adv. Mater. 33 (2021) 2105400, https://doi.org/10.1002/adma.202105400.

[152] Z.X. Ge, T.J. Wang, Y. Ding, S.B. Yin, F.M. Li, P. Chen, Y. Chen, Interfacial engineering enhances the electroactivity of frame-like concave RhCu bimetallic nanocubes for nitrate reduction, Adv. Energy Mater. 12 (2022) 2103916, https://doi.org/10.1002/aenm.202103916.